Submitted to: Remote Sensing of Environment (RSE)

# Retrieval of sun-induced fluorescence using advanced spectral fitting methods

*S. Cogliati[1*], W. Verhoef[2], S. Kraft[4,5], N. Sabater[3], L. Alonso[3], J. Vicent[3], J. Moreno[3], M Drusch[4], R. Colombo[1]*

*[1] Remote Sensing of Environmental Dynamics Lab., DISAT, University of Milano-Bicocca, P.zza della Scienza 1, 20126, Milano, Italy;*

*[2] University of Twente, Faculty of Geo-Information Science and Earth Observation (ITC), Hengelosestraat 99, P.O. Box 217, 7500 AE Enschede, The Netherlands;*

*[3] Department of Earth Physics and Thermodynamics, University of Valencia, Dr Moliner, 50, 46100 Burjassot - Valencia, Spain*

*[4] ESA-ESTEC, Keplerlaan 1, 2201 AZ Noordwijk, The Netherlands*

*[5] ESA-ESOC, Robert-Bosch-Strasse 5, 64293 Darmstadt, Germany*

Keywords: sun-induced Fluorescence, FLEX mission, retrieval algorithm, spectral fitting methods, full Fluorescence spectrum

***Corresponding author**: sergio.cogliati@unimib.it, +39-0264482860, Remote Sensing of Environmental Dynamics Lab., University of Milan-Bicocca, P.zza della Scienza 1, 20126, Milano, Italy

**Abstract**

The *FLuorescence EXplorer* (FLEX) satellite mission, candidate of ESA's 8th Earth Explorer program, is explicitly optimized for detecting the sun-induced fluorescence emitted by plants. It will allow consistent measurements around the $O_2$-B (687 nm) and $O_2$-A (760 nm) bands, related to the red and far-red fluorescence emission peaks respectively, the photochemical reflectance index, and the structural-chemical state variables of the canopy. The sun-induced fluorescence signal, overlapped to the surface reflected radiance, can be accurately retrieved by employing the powerful spectral fitting technique. In this framework, a set of fluorescence retrieval algorithms optimized for FLEX are proposed in this study. Two main retrieval approaches were investigated: i) the optimization of the spectral fitting for retrieving fluorescence at the oxygen absorption bands; ii) the extension of the spectral fitting to a broader spectral window to retrieve the full fluorescence spectrum in the range from 670 to780 nm. The accuracy of the retrieval algorithms is assessed by employing atmosphere-surface radiative transfer simulations obtained by coupling SCOPE and MODTRAN5 codes. The simulated dataset considers more realistic conditions because it includes directional effects, and the top-of-atmosphere radiance spectra are resampled to the current specifications of the *FLuORescence Imaging Spectrometer* (FLORIS) planned to serve as the primary instrument aboard FLEX. The retrieval accuracy obtained at the $O_2$-A band is strongly affected by directional effects, and better performance is found in cases where directional effects are lower. However, the best performing algorithms tested provided similar performance, the RMSE (RRMSE) is 0.044 mW $m^{-2}$ $sr^{-1}$ $nm^{-1}$ (6.2%) at the $O_2$-A band, 0.018 mW $m^{-2}$ $sr^{-1}$ $nm^{-1}$ (2.9%) at the $O_2$-B band, and 6.225 mW $m^{-2}$ $sr^{-1}$ (6.4%) for the spectrally integrated fluorescence emission. The promising results achieved open new perspectives extending fluorescence studies not only in limited absorption bands, but its spectral behavior in relation to different plant species, photosynthetic rates and stress occurrences.

## 1 Introduction

Satellite remote sensing provides fundamental data to study and monitor vegetation state variables and processes. Most Earth Observation missions rely on the analysis of the reflected radiance in the solar domain to derive bio-physical (i.e. fractional cover (FC), leaf area index (LAI)), and bio-chemical constituents of vegetation (i.e. chlorophyll, water and nitrogen). In the last few years, the remote sensing of sun-induced fluorescence (SIF) represents a novel approach to provide new insight into plant photosynthetic activity. SIF is a faint light signal released by the photosynthetic apparatus that plant canopies add continuously to the reflected radiance in the visible and near-infrared wavelength range. The strong interest and the various efforts ongoing by scientific community are prompted by the close link between SIF and the actual plant photosynthetic rate (Baker, 2008; Papageorgiou & Govindjee, 2004). The exploitation of this signal at continental and global scale for examining the atmosphere-vegetation carbon exchanges estimations (Guanter et al., 2014; Lee et al., 2013; Parazoo et al., 2014), and its parametrization into the Community Land Models (Lee et al., 2015), represent recent applications.

In the last few years, global scale maps of SIF in the far-red region have been generated by exploiting high spectral resolution sensors on board current space-borne mission, primarily devoted to atmospheric chemistry. Joiner et al., (2011), Frankenberg et al., (2011) and Guanter et al., (2012) produced the first global maps of far-red SIF by exploiting the data produced by the *TANSO Fourier Transform Spectrometer* on board the Japanese GOSAT satellite (Hamazaki et al., 2005; Kuze et al., 2009). Afterwards, global maps of far-red fluorescence have also been produced by exploiting the *SCanning Imaging Absorption SpectroMeter for Atmospheric CHartographY* (SCIAMACHY) aboard of ENVISAT (Joiner et al., 2012), and the *Global Ozone Monitoring Experiment 2* (GOME-2) flying on the operational European meteorological (MetOp) satellites (Joiner et al., 2013). Future advancements for the far-red SIF region are expected from NASA's OCO-2 (Frankenberg et al., 2014) launched in

July 2014, and the forthcoming *TROPOspheric Monitoring Instrument* (TROPOMI) to be aboard the Sentinel-5 Precursor (Guanter et al., 2015). The SIF retrieval algorithms from atmospheric space-borne satellites are mostly based on the analysis of the absolute in-filling of fluorescence in the solar Fraunhofer lines (740-755 nm). Even though the relative contribution of SIF is lower in such narrow lines compared to broader and deeper telluric oxygen bands, the main advantage of this approach relies in a simplified radiative transfer modeling of the atmospheric scattering and absorption effects in such spectral windows. The SIF global maps derived from the atmospheric sensors can be very useful for a global assessment of SIF, but their coarse spatial resolution (between few up to tens kilometers) do not provide optimal data to study terrestrial ecosystems. In fact, the heterogeneity of the natural land surface cannot be properly represented at these spatial resolutions in most of the cases. Furthermore, the spectral configurations of the existing atmospheric missions (mostly between 757-775 nm) do not allow the retrieval of red SIF, thus limiting the analysis to the far-red SIF only.

The *FLuorescence EXplorer* (FLEX) mission, candidate to the 8$^{th}$ Earth Explorer program, is currently under Phase A/B1 study by the European Space Agency (ESA). FLEX is explicitly optimized for detecting the SIF emitted by plants at a unique spatial resolution of 300 m (ESA, 2015). It will fly in tandem with the ESA's Sentinel-3 (S3) (Donlon et al., 2012) to take advantage of complementary measurements from the *Ocean and Land Color Instrument* (OLCI) and the *Sea and Land Surface Temperature Radiometer* (SLSTR). The FLEX/S3 tandem mission will provide numerous advantages including an accurate atmospheric correction, the consistent measurements of both red and far-red fluorescence peaks, the detection of the photochemical reflectance index (PRI) (Gamon et al., 1992), and estimation of bio-physical and bio-chemical canopy parameters. All these sources of information are essential in this mission for a better understanding and interpretation of sun-induced fluorescence, canopy variables and their relationships. Moreover, the canopy temperature delivered by S3 in combination with these information can allow to parametrize photosynthesis models to derive higher level products.

The *FLuORescence Imaging Spectrometer* (FLORIS) to fly aboard the FLEX satellite consists of two spectrometers explicitly designed to provide systematic high-resolution spectral radiance observations (0.3 nm) around the $O_2$-A (760 nm) and $O_2$-B (687 nm) absorption bands together with the continuous spectral coverage in the visible to near-infrared spectrum (500-780 nm, $\leq$ 3 nm). The technical specifications of FLORIS, in terms of spectral coverage, spectral resolution (SR), spectral sampling interval (SSI) and signal to noise ratio (SNR), are well suited for retrieving fluorescence by using spectral fitting methods (Mazzoni et al., 2012; Mazzoni et al., 2008; Mazzoni et al., 2010; Meroni et al., 2010). These methods make use of proper mathematical functions to simultaneously model the surface reflectance and fluorescence at different wavelengths within spectral windows confined to the oxygen absorption bands. However, FLORIS not only permits retrieving SIF at the two narrow $O_2$ bands with high accuracy, but it also offers a continuous spectral coverage over the entire spectral region where the fluorescence emission occurs. Taking advantage of this, spectral fitting approach can be further improved and tested over broader spectral windows with the aim of recovering the entire fluorescence emission spectrum. This could represent a relevant advancement because sun-induced fluorescence spectrum is a complex function which mainly depends on the specific emission of photosystem I ($PS_I$) and photosystem II ($PS_{II}$), and the successive re-absorption/scattering effects that occur at both leaf and canopy levels. The variability of SIF spectrum at leaf level in relation to different plant species, environmental conditions and plant's stress occurrence are documented in Agati, (1998) and Van Wittenberghe et al., (2013). Therefore, the possibility of retrieving the fluorescence spectrum opens novel and promising perspectives to have a better understanding of fluorescence in relation to photosynthesis and other canopy state variables.

In this framework, the main aim of this study is to develop and testing SIF retrieval algorithms optimized for FLORIS, and suitable for similar high-resolution sensors, based on Spectral Fitting Methods. The specific objectives consist in: i) optimizing existing SFMs in confined spectral windows around the $O_2$ absorption bands; and ii) developing a novel retrieval algorithm which allows estimating SIF spectrum. The paper is structured as follows: section 2 describes the FLEX mission providing technical details on the FLORIS instrument. Section 3 describes the radiative transfer equations used, the SIF retrieval algorithms developed, and the metrics used for evaluating the retrieval accuracy. Section 4 shows and discuss the results with emphasis on the impact of atmosphere-surface directional effects. Section 5 describes a number of indices that can be derived from FLEX. The main findings of the study are summarized in section 6.

## 2 The FLEX/S3 tandem mission

The FLEX satellite is expected to fly in tandem with the Sentinel-3 in a Sun-synchronous orbit at an altitude of about 815 km to deliver imagery at 300 m spatial resolution with a swath of 150 km (ESA, 2015). The revisit time will be 27 days at the Equator and more frequent acquisitions (~19 days) over high latitudes due to orbital overlaps. The lifetime foreseen of the mission is 3.5 years. The *FLuORescence Imaging Spectrometer* (Kraft et al., 2012, 2013), on board of FLEX, is a pushbroom imaging spectrometer designed to detect canopy fluorescence and reflectance within a spectral range between 500 and 780 nm. The current configuration of the FLORIS instrument consists of two spectrometers: i) the *Narrow Band Spectrometer* (NBS) which provides high-resolution radiance in defined spectral ranges around the $O_2$-A and $O_2$-B absorption bands, ii) the *Wide Band Spectrometer* (WBS) characterized by a broader spectral coverage from 500 to 740 nm, with a lower spectral resolution. The spectral bands are then resampled according to a defined binning scheme providing the proper SR, SSI and SNR over the different spectral ranges. The resulting characteristics expected for a typical spectral radiance observation by FLORIS are reported in Table 1. The required SNR values synthetized in the table refer to the spectral bands, therefore the expected actual values will be higher after the spectral binning.

<Table 1>

The combination of NBS and WBS spectra will provide both the high SR for fluorescence retrieval at the $O_2$ bands, and a broader spectral coverage, at the same time (Figure 1). This particular combination of variable SRs, SSI, and the binning-scheme will provide an unprecedented SNR, which is one key factor ensuring accurate retrieval of SIF.

<Figure 1>

# 3 Materials and Methods

## 3.1 Radiative transfer simulations

A dataset of radiative transfer (RT) simulations has been initially created to develop the retrieval algorithms and to assess their performances. It consists of fluorescence, reflectance and total upward radiance at top of atmosphere (TOA) and bottom of atmosphere (BOA, assumed to be equivalent to TOC, top-of-canopy) calculated by coupling the *Soil Canopy Observation Photosynthesis Energy balance* (SCOPE) (Van Der Tol et al., 2009) with the *MODerate resolution atmospheric TRANsmission* (MODTRAN) RT models. In particular, the forward model used relies on the four-stream radiative transfer theory (Verhoef & Bach, 2007, 2012) with the addition of the direct and diffuse fluorescence fluxes (Verhoef et al., 2014). It represents an accurate, efficient and relatively simple way to describe the radiative transfer interactions of the Earth's surface–atmosphere system. The surface-atmosphere

RT interactions and the subsequent propagation to the top of the atmosphere ($L^{TOA}$) are defined in the following radiative transfer equation, Eq. 1.

$$
\begin{aligned}
L^{\mathrm{TOA}} = {} & \rho_{so}\frac{E_s^0\cos\theta_s}{\pi} \\
& + \left[\frac{\tau_{ss}r_{so}E_s^0\cos\theta_s}{\pi} + SIF_s + \frac{(\tau_{sd}+\tau_{ss}\overline{r_{sd}}\rho_{dd})E_s^0\cos\theta_s/\pi + \overline{SIF_d}\rho_{dd}}{1-\overline{r_{dd}}\rho_{dd}}r_{do}\right]\tau_{oo} \\
& + \left[\frac{(\tau_{sd}\overline{r_{dd}}+\tau_{ss}\overline{r_{sd}})E_s^0\cos\theta_s/\pi + \overline{SIF_d}}{1-\overline{r_{dd}}\rho_{dd}}\right]\tau_{do}
\end{aligned}
\qquad \text{Eq. 1}
$$

$L^{TOA}$ is therefore composed of three additive terms (the 3 lines on the right-hand side of Eq. 1) which are referred to as the atmospheric path radiance, the target's surface radiance and the adjacency effect, respectively. The surface reflectance is modelled by four terms: $r_{so}$ is the target bi-directional reflectance factor (BRF), $r_{do}$ the target hemispheric-directional reflectance factor (HDRF), $\overline{r_{sd}}$ the spatially filtered directional-hemispherical reflectance factor (DHRF) of the surrounding, $\overline{r_{dd}}$ the spatially filtered bi-hemispherical reflectance (BHRF) of the surrounding (c.f. Nicodemus et al., (1977) for a description of used reflectance quantities). The term $\rho_{so}$ is the atmospheric bi-directional reflectance and $\rho_{dd}$ is the spherical albedo at the bottom of the atmosphere. The term $\tau_{ss}$ is the direct atmospheric transmittance in the direction of the sun, $\tau_{oo}$ is the direct atmospheric transmittance in the direction of viewing, $\tau_{sd}$ the diffuse atmospheric transmittance for solar incidence, and $\tau_{do}$ the directional atmospheric transmittance for diffuse incidence. The quantity $E_s^0$ is the extra-terrestrial solar spectral irradiance on a plane perpendicular to the sunrays, and $\theta_s$ is the local solar zenith angle (SZA). $SIF_s$ is the sun-induced fluorescence radiance of the target in the observer's direction and $\pi SIF_d$ the hemispherical fluorescence flux of the surroundings. The RT simulations consider a homogenous 1-D target in the horizontal plane, and the over bar indicates the spatial filtering of the terms related to the infinitely extended surrounding area.

Strictly, Eq. 1 is only valid for monochromatic radiation because the atmospheric quantities $\rho_{so}$, $\rho_{dd}$, $\tau_{ss}$, $\tau_{oo}$, $\tau_{sd}$, and $\tau_{do}$ are strongly modulated by narrow absorption lines due to various gases in the atmosphere, and therefore they are strongly correlated in spectral regions where many absorption lines are present. Consequently, the mean value of a product of these quantities over a finite spectral interval (i.e. integration of radiance in the sensor spectral bands) is not equal to the product of the mean values of the individual quantities. Hence, the products of the different atmospheric quantities needed are formed and stored at high spectral resolution (Verhoef et al., 2014), before the convolution to the sensor spectral band. The set of atmospheric transfer functions required by Eq. 1 is summarized in Figure 2.

<Figure 2>

Based on these transfer functions, Eq. 1 can be rewritten as (Eq. 2).

$$L^{TOA} = t_1 \left[ t_2 + t_8 r_{so} + \frac{t_9 + t_{14}\overline{r_{sd}}}{1 - \overline{r_{dd}}\, t_3} r_{do} + \frac{t_{10}\overline{r_{sd}} + t_{11}\overline{r_{dd}}}{1 - \overline{r_{dd}}\, t_3} \right] + t_6 SIF_s + \left[ \frac{\overline{SIF_d}(t_7 + t_{13} r_{do})}{1 - \overline{r_{dd}}\, t_3} \right] \qquad \text{Eq. 2}$$

The corresponding upward radiance at the bottom of atmosphere $L^{BOA}$ is calculated using a scheme in which some transfer functions represent single-way ($t_4$ and $t_5$) instead of two-way transmittances:

$$L^{BOA} = t_1 \left[ t_4 r_{so} + \frac{t_5 + t_{12}\overline{r_{sd}}}{1 - \overline{r_{dd}}\, t_3} r_{do} \right] + SIF_s + \left[ \frac{\overline{SIF_d}\, t_3 r_{do}}{1 - \overline{r_{dd}}\, t_3} \right] \qquad \text{Eq. 3}$$

Eq. 3 can also be used to calculate the upwelling radiance from the White Lambertian Reference ($L^{WLR}$) panel by setting the reflectance terms from the target $r_{so}$ and $r_{do}$ equal to one and the target fluorescence equal to zero. This quantity represents the global (direct and diffuse) incoming radiance at ground level including the adjacency effects from the surrounding.

$$L^{WLR} = t_1 \left[ t_4 + \frac{t_5 + t_{12}\overline{r_{sd}}}{1 - \overline{r_{dd}}\, t_3} \right] + \left[ \frac{\overline{SIF_d} t_3}{1 - \overline{r_{dd}}\, t_3} \right] \qquad \text{Eq. 4}$$

The ratio of $L^{BOA}$ and $L^{WLR}$, as measured by ground-based measurements, is the surface apparent reflectance ($\rho_{app}$), which includes both reflected and fluorescence radiance (Eq. 5). The surface reflectance free of the fluorescence contribution ($\rho$), (Eq. 6), represents the reference value of the retrieval algorithms.

$$\rho_{app} = \frac{L^{BOA}}{L^{WLR}} \qquad \text{Eq. 5}$$

$$\rho = \frac{L^{BOA} - SIF_s}{L^{WLR}} \qquad \text{Eq. 6}$$

The four surface reflectance terms, $SIF_s$ and $SIF_d$ spectra were simulated by using version 1.40 of the SCOPE model. The RT calculations in the solar-reflective domain are performed in SCOPE with a spectral sampling and resolution of 1 nm over the 400–2400 nm range. The atmospheric transfer functions were instead derived from the MODTRTAN 5.2.1 code (Berk et al., 2011). Different atmospheric conditions (i.e., visibility, humidity, aerosol type, profile etc.) were simulated at 1 cm$^{-1}$ spectral sampling over the 400–50000 nm range, and the atmospheric transfer functions were calculated by using the MODTRAN Interrogation Technique (MIT) (Verhoef & Bach, 2012).

In summary, the database consists of 31 cases simulated with different soil, leaf, canopy and atmospheric parameters (Table 2). The values reported in the column labeled “medium” are used to simulate case n° 19, which refers to a typical scenario in terms of vegetation and atmospheric parameters. The other cases are deviations from the typical scenario and they are obtained by changing mostly one parameter at a time. In particular, the cases 1-18 are deviations of surface parameters, while cases 20-31 correspond to deviations of the atmospheric conditions, including SZA. The MODTRAN simulations were done independently, but the SCOPE parameters were set-up consistently with MODTRAN at corresponding values (indicated in Table 2 in the column ‘Coupling’). It should be noted that this novel RT dataset includes a fundamental advancement, since for the first time, it includes a realistic modelling of the canopy-atmosphere directional effects by considering the four reflectance terms and their coupling with the atmospheric functions. Nadir viewing was used for all the simulations, which is close to reality for the satellite observations. The resulting spectra were convolved with the FLORIS-NBS and FLORIS-WBS instruments spectral response functions, and they were binned according to the current specifications provided by ESA. A Gaussian distributed noise, of which the variance was linearly related to the $L^{TOA}$ intensity at the different wavelengths, was added to the TOA radiances (Verhoef et al., 2014) to simulate the noise levels expected for FLORIS. The variabilities of surface $\rho$, $SIF$ and the TOA radiance simulated in the FLORIS configuration are depicted in Figure 3.

The FLEX/S3 tandem mission will allow the exploitation of the additional data available from Sentinel-3 (e.g., in the blue and the cirrus bands) to provide a highly accurate atmospheric correction. The mission configuration is well suited to consider a two-step retrieval approach which considers a preliminary correction of the atmospheric effects followed by the decoupling of the SIF and reflectance. The two successive steps are executed independently starting from the TOA radiance to calculate the canopy fluorescence and reflectance. Specifically, the TOA is converted to the BOA radiance by the atmospheric correction calculations, and then the fluorescence and reflected radiance are decoupled from the BOA spectra. This approach has the advantage of a limited number of model parameters to be estimated in the two distinct retrieval processes, thus providing stable results. In this way, the sources and the magnitudes of the retrieval error for the atmospheric correction and the following fluorescence retrieval can be better quantified and understood. It must be noted that the retrieval of the atmospheric parameters, which includes a detailed coupling between the FLEX and S3 data, is not considered in this work. A slightly simplified, but still relatively accurate, forward propagation model (Eq. 7) for the TOA radiance is considered in this study as baseline for simulating the correction of atmospheric effects (Verhoef et al., 2014). The right-hand side of Eq. 7 contains a linear combination of the four reflectance terms and the two fluorescence terms in the numerator.

$$L^{TOA} \approx \left[ t_1 t_2 + \frac{t_1\left(t_8 r_{so} + t_9 r_{do} + t_{10}\overline{r_{sd}} \ + t_{11}\overline{r_{dd}}\right) + t_6 SIF_s + t_7 SIF_d}{1 - t_3\overline{r_{dd}}} \right] \qquad \text{Eq. 7}$$

The atmospheric correction applied is based on the assumption of a uniform and Lambertian surface with a reflectance ρ and a fluorescent radiance SIF. The atmospheric correction is applied considering the following quantities:

$$L_0 = t_1 t_2 \qquad \text{Eq. 8}$$

$$g\rho = t_1\left(t_8 r_{so} + t_9 r_{do} + t_{10}\overline{r_{sd}} \ + t_{11}\overline{r_{dd}}\right) \qquad \text{Eq. 9}$$

$$tSIF = t_6 SIF_s + t_7 SIF_d \qquad \text{Eq. 10}$$

$$S = t_3 \qquad \text{Eq. 11}$$

where the path radiance for a black surface with zero albedo, $L_0$, is given by the $t_1 t_2$ product (Eq. 8), $g$ is the gain factor to obtain TOA radiance, $\rho$ is the “effective” reflectance, i.e. a weighted average of the four reflectance terms (Eq. 9), $tF$ is the “effective” transmitted fluorescence (Eq. 10), and $S$ is the atmospheric spherical albedo (Eq. 11). With these quantities, the simplified atmospheric forward model can be rewritten as:

$$L^{TOA} \approx L_0 + \frac{g\rho + tSIF}{1 - \rho S} \qquad \text{Eq. 12}$$

The surface apparent reflectance $R_{ac}$ (i.e. reflectance and SIF contributions) after atmospheric correction (under the assumption of zero *SIF*) can be obtained by solving $\rho$ from Eq. 12 for *SIF* = 0, and turns out to be given by

$$R_{ac} = \frac{g\ \rho + t\ SIF}{g + S\ t\ SIF} \qquad \text{Eq. 13}$$

The resulting $R_{ac}$ is practically equal to a weighted average of the four surface reflectance factors, with a small contribution due to fluorescence from the target and the surrounding. The contribution from fluorescence will be relatively larger in atmospheric absorption bands, since $t$ is less attenuated by absorption than $g$. After the atmospheric correction, considering a "perfect knowledge" of the atmospheric transfer functions, the best available approximation for the radiance of the white Lambertian reference is given by Eq. 14.

$$L^{WLR} = \frac{t_1(t_4 + t_5)}{1 - SR_{ac}} \qquad \text{Eq. 14}$$

Finally, the BOA radiance is obtained from Eq. 15 by combining Eq. 13 and Eq. 14. This means that $L^{BOA}$ derives directly from $L^{TOA}$ once the atmospheric parameters are known. In this way, the noise in $L^{TOA}$ is also propagated into $L^{BOA}$.

$$L^{BOA} = R_{ac} L^{WLR} \quad \text{Eq. 15}$$

It should be noted that the two-step procedure described above was applied in the numerical experiments discussed in this paper. However, on the basis of Eq. 12 one could also develop a single step approach, in which measured TOA radiances would be fitted using Eq. 12 with atmospheric transfer functions and modeled spectral curves of surface reflectance and fluorescence as inputs. In a single step approach no atmospheric correction has to be carried out, only atmospheric characterization, and the assumptions usually made for correction approaches (i.e. uniform and Lambertian surface, homogeneous atmosphere, etc.) are no longer necessary, leading to greater flexibility and robustness.

### 3.2 Fluorescence retrieval

Once the TOA radiance from FLORIS is converted to BOA after the atmospheric correction, the radiance spectra are now composed of the additive contributions of fluorescence and sun reflected radiance (Eq. 16).

$$L^{BOA}(\lambda) = \rho L^{WLR}(\lambda) + SIF(\lambda) \quad \text{Eq 16}$$

The decoupling of the two terms is then achieved by using the spectral fitting approach. Basically, it consists in the optimization of the fit between modelled and measured spectra of both fluorescence and reflectance by adjusting the mathematical functions used to describe SIF and $\rho$ spectral behaviors within the defined spectral window. The parameters of the mathematical functions used for SIF and ρ are estimated through a least square nonlinear curve-fitting optimization technique that minimizes the cost function in Eq. 17. The MATLAB function LSQCURVEFIT was used to perform the optimization. This routine allows to include upper and lower bounds for model parameters excluding solutions without a physical meaning (i.e. negative SIF and ρ).

$$\min \sum \left(L^{BOA}(\lambda) - SIF(\lambda) - \rho(\lambda) L^{WLR}(\lambda)\right)^2 \qquad \text{Eq. 17}$$

The usage of a large number of spectral bands has many advantages allowing estimation of a larger number of model parameters that describe the spectral variables behavior, and reduce the impact of instrumental noise. A source of error in these SIF retrieval methods could be due to the wrong assumptions (i.e. linear, polynomial) about spectral functions used in modelling SIF and ρ. In general, the use of functions with a larger number of parameters increases the modelling capability of the spectral variable of interest. It is usually required for modelling broader spectral windows, and it is particularly relevant to account for sharp spectral features within the considered spectral range. On the other hand, it could lead to undesired problems like data over-fitting (i.e., the fitting model does not describe the variable of interest but the random error) or ill-posed numerical inversions. For these reasons, an optimal balance between model parameters, spectral window, and retrieval accuracy is needed and it is assessed in this study.

The spectral fitting method has been applied in the narrow spectral range provided by the FLORIS-NBS (hereafter named SFM according the terminology originally proposed in Mazzoni et al., (2012); Meroni et al., (2010)) to retrieve fluorescence in confined spectral windows centered at the $O_2$-bands, while a novel spectral fitting based algorithm aimed at the retrieval of the full fluorescence emission spectrum and a series of derived products is hereafter referred to as *SpecFit*.

### 3.2.1 Fluorescence retrieval at the $O_2$ bands (SFM)

The high resolution spectra around the two $O_2$ absorptions from the FLORIS-NBS instrument are particularly indicated for the retrieval of SIF by exploiting spectral fitting methods (SFM). The rationale behind the exploitation of narrow spectral regions, characterized by strong absorptions, resides in the higher contribution of SIF with respect to the total radiance. For this reason, the SFM algorithms are focused on the detection of SIF at the $O_2$ bands or, at least, in relatively narrow regions around the main absorption features. The use of such fitting windows permits to reduce the impact of instrumental noise (which is higher in the absorption bands), and to exploit additional absorptions features nearby (i.e. the solar Fraunhofer lines in the 740-759 nm range). The modelling of SIF and $\rho$ as a function of wavelengths is simpler in relatively narrow spectral ranges, but less spectral information is used in the decoupling. This is particularly true at the $O_2$-A band where reflectance is a smooth function, while it is more difficult at $O_2$-B due to the rising of the red-edge reflectance. In fact, the $O_2$-B band is very close to the red-edge transition and it is located adjacent to the maximum of the fluorescence emission peak (684-685 nm). Such behavior makes the modelling of the spectral functions difficult in this region. Moreover, the typical radiance levels for vegetated surfaces in the red spectrum (i.e., chlorophyll absorption) are generally much lower than in the near-infrared (around the $O_2$-A band) and consequently the SNR is worse. On the other hand, the relative contribution of SIF to the total radiance is larger in this spectral region. To evaluate all these aspects, two different spectral windows centered at the main oxygen absorption bands (Table 3) were considered for evaluating these factors. In this setting, narrow spectral windows within the FLORIS-NBS spectrum are exploited to retrieve SIF by SFM.

< Table 3>

A total of 54 combinations of spectral functions were tested to predict fluorescence and reflectance (Table 4). The $\rho$ models are based on polynomial functions (P), Legendre (L) polynomials, and piecewise cubic spline (S) with different knots (i.e., 2, 4, 6 knots). The SIF is represented with both polynomial (P), Legendre (L) and spline (S) functions (for models IDs 1-9) and by using Gaussian, Lorentzian and Voigt profiles (for model IDs 10-18). The models 1-9 for each class are obtained by combining functions with a different polynomial order (i.e., from $1^{st}$ to $3^{rd}$ degree) or number of knots for the cubic splines. The models 10-18 were obtained by considering polynomials for reflectance and Gauss, Lorentz and Voigt profiles to model fluorescence.

<Table 4>

### 3.2.2 Retrieval of the full fluorescence spectrum (SpecFit)

With this approach we extend the spectral fitting technique over the entire spectral region where the fluorescence emission occurs. It relies on the inversion of the radiance spectrum in the red to far-red spectral region for estimating the full fluorescence spectrum in the 670-780 nm range. Also this approach takes advantage of the spectral configuration of FLORIS instrument. In particular, the high resolution spectra around the $O_2$ bands from FLORIS-NBS are joined in the red-edge by the lower resolution spectra from FLORIS-WBS in order to obtain continuous spectral coverage. The idea underlying this algorithm is almost the same as the spectral fitting described earlier, but the mathematical functions used to predict SIF and ρ spectral behaviours in such a broader spectral window are more complex.

The piecewise cubic spline was selected to reproduce the reflectance signature in the red to far-red spectral region. The two red and far-red SIF emission peaks were modelled using different combinations of Gaussian, Lorentzian and Voigt profiles. Generally, the fitting of the red peak is simpler because almost all of the contribution is due to the $PS_{II}$ only; $PS_{I}$ only contributes to the red-edge tail of the first (red) emission peak (Franck et al., 2002). This fact results in an almost stable position and width of the red peak. On the contrary, the modelling of the far-red peak is more difficult because there are both $PS_{II}$ and $PS_{I}$ contributions, and these two act differently. Depending on the relative contribution of fluorescence emitted by $PS_I$ or $PS_{II}$, the wavelength of the maximum emission shifts over several nanometers (i.e., up to 5-6 nm) and in some cases the peak shows an asymmetric behavior. Two different implementations were considered to achieve an accurate fitting of the full SIF spectrum: i) the Lorentzian and Gaussian functions were used to model red (684 nm) and far-red (740 nm) peaks, respectively; ii) two Voigt functions with an asymmetry parameter were used for both peaks. The first implementation method has the advantage of being more robust because a total of 6 parameters are used (i.e. 3 for each emission peak). However, it must be noted that Lorentzian and Gaussian functions do not provide as much flexibility to obtain accuracy in modelling the peaks' spectral profiles, as do the Voigt functions. Unfortunately, the computation of the Voigt function is time expensive due to the convolution between the Gaussian and Lorentzian functions. This point is critical when the functions must be computed several times within the iterative optimization process. For this reason the so-called pseudo-Voigt function, computed as a weighted combination of the Lorentzian and Gaussian functions, was selected for modelling each one of the two fluorescence emission peaks. The first term of the pseudo-Voigt function represents the Lorentzian contribution, while the second term represents the Gaussian contribution. The full SIF emission spectrum is therefore the sum (Eq. 18) of the two pseudo-Voigt functions. The pseudo-Voigt functions were used to model the red (Eq. 19) and far-red (Eq. 20) peaks respectively. The far-red peak includes also an additional parameter (Eq. 21) to account for the peak asymmetry as proposed in Stancik & Brauns, (2008).

$$SIF(\lambda) = SIF_{far-red}(\lambda) + SIF_{red}(\lambda) \quad \text{Eq. 18}$$

$$SIF_{red}(\lambda) = f\frac{\mu}{\left(\frac{\lambda-\lambda_0}{\sigma(\lambda)}\right)^2+1} + (1-f)\ \mu\exp\left(-\frac{(\lambda-\lambda_0)^2}{2\sigma(\lambda)^2}\right) \quad \text{Eq. 19}$$

$$SIF_{far-red}(\lambda) = f\frac{\mu}{\left(\frac{\lambda-\lambda_0}{\sigma(\lambda)}\right)^2+1} + (1-f)\ \mu\exp\left(-\frac{(\lambda-\lambda_0)^2}{2\sigma_{asym}(\lambda)^2}\right) \quad \text{Eq. 20}$$

$$\sigma_{asym}(\lambda) = \frac{2\sigma}{(1+\exp\left(a(\lambda-\lambda_0)\right))} \quad \text{Eq. 21}$$

### 3.3 Error estimation

A number of statistical indicators were used to evaluate the performance of the retrieval algorithms in a consistent way. The accuracy was assessed by comparing the reference simulated SIF and ρ against the retrieved values at different λ. The statistical indexes considered in this study are the Root Mean Square Error (RMSE) (Eq. 22) which quantifies the amount by which an estimation differs from the assumed true value of the quantity, and the Relative RMSE (RRMSE) that represents the percentage of error with respect to the actual values (Eq. 23). The absolute difference ($SIF_{diff}$) between simulated and retrieved fluorescence (Eq. 24) provides information on whether retrieved fluorescence is underestimated or overestimated. Finally, a comparison was conducted of the coefficient of determination ($r^2$) between simulated and retrieved values.

$$RMSE = \sqrt{\frac{\sum_{\lambda=1}^{n}(SIF(\lambda)\ - SIF_{ret}(\lambda))^2}{n}} \qquad \text{Eq. 22}$$

$$RRMSE = \sqrt{\frac{\sum_{\lambda=1}^{n}\left(\frac{SIF(\lambda) - SIF_{ret}(\lambda)}{SIF(\lambda)}\right)^2}{n} * 100} \qquad \text{Eq. 23}$$

$$SIF_{diff} = \int_{\lambda} SIF_{ret}(\lambda)d\lambda - \int_{\lambda} SIF(\lambda)d\lambda \qquad \text{Eq. 24}$$

# 4 Results and Discussions

## 4.1 Fluorescence at the $O_2$ bands

Although different spectral ranges were tested (data not shown), the broader range indicated in Table 3 was the most efficient for the retrieval of fluorescence. This is probably due to the additional information content in the broader spectral window (i.e., inclusion of solar Fraunhofer lines), and at the same time, reducing the impact of instrumental noise by using a larger set of spectral channels. The overall accuracy for the 31 cases in shown in Figure 4.

<Figure 4>

The overall accuracy depends on the performances of the spectral functions used for representing SIF and ρ in the numerical inversion. As observed in previous studies, the reflectance around the $O_2$-A band is generally smooth and most polynomials and Legendre polynomials of 2$^{nd}$ and 3$^{rd}$ order and piecewise cubic splines produce a suitable fit of the reflectance spectra (Mazzoni et al., 2012; Meroni et al., 2010). On the other hand, it can be observed that polynomial functions do not produce as accurate results in modelling the fluorescence spectrum when compared to peak-like functions (i.e., Gaussian, Lorentzian and Voigt). In fact, the SFM versions 1-9 resulted in larger RMSE values, with the only exception being the piecewise cubic spline at the $O_2$-A band. In summary, better accuracy was achieved by the SFM version "18-Spline" which makes use of piecewise cubic spline and Voigt functions to model reflectance and fluorescence respectively.

A different situation happened at the $O_2$-B band, where sharp variations of both reflectance and fluorescence occur. The piecewise cubic spline and the Voigt spectral functions enabled SIF to be retrieved with a proper accuracy at the $O_2$-B band using the SFM version "18-Spline". Since the same functions provided higher accuracy in both the $O_2$-A and $O_2$-B bands, the "18-Spline" should be considered as the best candidate for further implementation for FLEX. The further analysis hereafter refers to this specific SFM version.

The analysis of the retrieval performances for the different RT simulations is fundamental assessing the sensitivity of the retrieval algorithm to specific parameters in the forward model. The retrieval accuracies for each one of the different 31 RT simulations (Figure 5) are not significantly affected when surface or atmospheric parameters are modified. For the $O_2$-A band, an average RMSE lower than 0.1 $mWm^{-2}sr^{-1}nm^{-1}$ (RRMSE% < 8) was found for almost all cases, with the exception of simulations 15-18 and 31 where significantly better performances were found with RMSEs < 0.025 $mWm^{-2}sr^{-1}nm^{-1}$ (RRMSEs% < 1). These cases represent extreme LAI values (0.5 and 6.0 $m^2/m^2$ for cases 15 and 16 respectively), leaf angle distribution (planophile and erectophile for cases 17, 18 respectively) and very low solar zenith angles (case 31). The light penetration within the canopy, and the successive interaction with soil, are key factors which cause most of the canopy directional effects. In fact, low/high LAI values or erectophile/planophile leaves distributions determinate that light rays mostly interact with soil/canopy only. On the contrary, intermediate cases show larger directional effects caused by a larger mixing between the different soil/canopy contributions. The $SIF_{diff}$ index shows that in the best cases the SIF values at $O_2$-A band are generally underestimated by about -0.1 $mWm^{-2}sr^{-1}nm^{-1}$, which is a reasonable error in line with the mission requirements. The results obtained at the $O_2$-B for the different RT simulations are more similar, and the RMSE is generally lower than 0.05 $mWm^{-2}sr^{-1}nm^{-1}$ (RRMSEs% < 4) and a slight underestimation is observed.

<Figure 5>

The agreement between the simulated and retrieved SIF and ρ spectra for one of the better result (case 17) and for one of the worst results (case 30) are shown in Figure 6. It can be observed that for the worst case, the true reflectance is not smooth at the $O_2$-A band but it presents oscillations. The latter are produced by the coupled canopy-atmosphere directional effects when the four reflectance terms from SCOPE are coupled with the atmospheric functions to obtain the total canopy reflectance ρ. This effect produces most of the error in the retrieval of the reflectance spectra and consequently the SIF retrieval results are a bit underestimated at the $O_2$-A.

<Figure 6>

This effect can be also observed by evaluating the different reflectance terms simulated in SCOPE. Figure 7 shows the variability of the four reflectance terms for cases 17 and 30. The four reflectance terms simulated with SCOPE are more similar for case 17 and for all the other cases where better retrieval performances were found. On the contrary, the variability observed for case 30 indicates a canopy with a strong anisotropic reflectance, which causes difficulties in the fluorescence estimations. This is explained by the fact that the depth of the atmospheric absorption depends on the path-length followed by photons from the sun via the ground to the sensor. The shortest and most direct photon path through the atmosphere corresponds to the sun-target-sensor route. Therefore the $r_{so}$ corresponds to the shortest photon path and the shallowest absorption depth. Reflectance factors involving diffuse fluxes like the $r_{do}$, $r_{sd}$ and $r_{dd}$ correspond to the reflection of sky radiation by the target or to hemispherically reflected radiation by the surroundings. These are always associated to longer photon paths through the atmosphere, and therefore to deeper absorptions. If the $r_{so}$ term is higher than the other reflectance terms, shorter photon paths receive more weight, with less deep atmospheric absorption, which contributes to the in-filling and therefore SIF will be underestimated. If the other reflectance terms are higher than $r_{so}$, then long photon paths receive more weight, due to deep atmospheric absorption, which will work as the negative of infilling. The in-filling by fluorescence can therefore be confused with the apparent positive or negative in-filling caused by directional effects. These effects should be considered in further retrieval algorithms because they have a large impact on the overall accuracy. For example, the spectral fitting approach can be improved considering both direct and diffuse canopy reflectance. Alternatively, Verhoef et al., (2014) proposes the numerical inversion of a simplified version of SAIL canopy RT model to represent the different direct and diffuse reflectance terms.

<Figure 7>

A typical example of the reflectance and fluorescence retrieval at the $O_2$-B band is shown in Figure 8. Although fluorescence and reflectance have a more complex behaviors in the spectral window considered, the Voigt and the piecewise cubic spline functions are able to fit accurately the two spectral components. The directional effects seem to be less significant in this region probably due to the lower magnitude of oxygen in this absorption band.

<Figure 8>

## 4.2 Full Fluorescence spectrum

The *SpecFit* approach is supposed to provide the full fluorescence emission spectrum by combining the FLORIS-NBS and –WBS radiance observations. The number of knots to be used in the piecewise cubic spline to accurately fit the surface reflectance signatures has been initially evaluated by considering an increased number of knots (Figure 9). The results show that 15 knots can properly model the reflectance in the broad spectral region considered in *SpecFit*. In those cases of reflectance signatures with low chlorophyll content or LAI values (i.e., characterized by a weaker red-edge transition), 12 knots seem to be enough, but in order to assure higher accuracies for all the considered cases 15 knots are preferred.

<Figure 9>

The RMSE and RRMSE at the $O_2$-A, $O_2$-B and for the entire full SIF spectrum are shown in Figure 10. The average RMSE is generally lower than 0.15 mW $m^{-2}$ $sr^{-1}nm^{-1}$ (RRMSE 10%), and slightly better performances are found for cases 15-18 and 31. These results are somewhat close to those found at the $O_2$-A band by the SFM approach in narrower spectral windows. In fact, the overall accuracy is similar (at least only slightly worse due to the broader spectral window), and more accurate results are found for cases characterized by weaker directional effects. Therefore, the results suggest that the surface-atmosphere directional effects at the $O_2$-A band also have a large impact on the retrieval accuracy of *SpecFit* algorithm.

<Figure 10>

In spite of the difficulties in modeling ρ and SIF in a broader spectral window, the retrieved spectra well represent the target (i.e. input from SCOPE). The full SIF spectrum retrieval results for one of the better cases (case 17) and for the worst (case 30) are reported Figure 11. The reflectance is well modelled in the entire spectrum and it is close to the target spectrum. Also the spectral behavior of retrieved fluorescence is similar to the target, but in some cases slight underestimations occurred mostly driven by the directional effects at the $O_2$-A band. It must be noted that the different shapes of the fluorescence strictly depend on the different relative contributions of $PS_I$ and $PS_{II}$ to the total fluorescence spectrum and on the leaf chlorophyll content.

<Figure 11>

## 4.3 Comparison of the retrievals

The scatterplot between target and retrieved SIF values allow a final performance evaluation of the different retrieval algorithms proposed. The two retrieval approaches show an overall good agreement at 760 nm, 687 nm, and for the spectrally integrated spectrum for all 31 cases (Figure 12). The slopes at 760 nm are slightly different from the 1:1 line, and the intercepts have slightly negative values that are due to the general underestimation of SIF at the $O_2$-A band caused by the surface-atmosphere directional effects.

<Figure 12>

A comprehensive summary of the retrieval performances relative to both retrieval methods is reported in Table 5. The goodness of fit in terms of the adjusted $r^2$ are 0.97-0.98 for the $O_2$-A band. The RMSE (RRMSE) 0.037 mW $m^{-2}$ $sr^{-1}$ $nm^{-1}$ and 0.044 mW $m^{-2}$ $sr^{-1}$ $nm^{-1}$ (7.4% and 6.2%) respectively for SFM and *SpecFit*. For the $O_2$-B, the retrieval performances at 687 nm are generally better, the slope parameter is closer to 1.0, the $r^2_{adj}$ 0.99, and the general RMSE (RRMSE) 0.018 mW $m^{-2}$ $sr^{-1}$ $nm^{-1}$

(3.0%). It must be noted that results obtained at the oxygen absorption bands by *SpecFit* are a bit better than SFM. This is because the applied fitting over a broader spectral window reduces the directional effects, and instrumental noise, which have a higher impact within the strong absorption bands. Finally, the results achieved by *SpecFit* for the spectrally integrated SIF values in the 670-780 nm spectral range show an overall RMSE (RRMSE) of 6.225 mW $m^{-2}$ $sr^{-1}$ (6.4%).

<Table 5>

The overall results presented here are analogous with respect to the earlier works based on the spectral fitting methods (M. Mazzoni et al., 2012; M. Meroni et al., 2010) at the $O_2$ bands. The piecewise cubic spline and Voigt spectral functions, employed to predict reflectance and fluorescence respectively, were also identified as best candidates in the previous work by Mazzoni et al., 2012. However, the quantitative comparison is difficult because the radiative transfer simulations used are very different. In fact, the four-way RT forward model used in this work includes a more realistic representation of the surface directional effect which allowed us to isolate directional effects as the major source of error in the retrieval, especially at the $O_2$-A band. For such reason, only those cases which characterize low directional effects (cases 15-18, 31) should be used in the comparison with earlier studies. Furthermore, the instrument specifications in terms of spectral resolution, sampling interval, and SNR assumed in previous works were generally better. The comparison with the results achieved from other methods (Frankenberg et al., 2011; Guanter et al., 2010; Guanter et al., 2012, 2014; Joiner et al., 2011) is even more difficult because the retrieval errors reported also include the additional uncertainty associated with atmospheric compensation. The comparison with Zhao et al., (2014) is also difficult because the results reported are in absolute values (i.e., RMSE) which are dependent on the specific dataset of radiative transfer simulation used.

## 5 Fluorescence derived indices from FLEX mission

A number of products are planned to be delivered from the FLEX mission. The Level 1 products will consist of calibrated and geometrically corrected top-of-atmosphere radiances. The Level 2 products will be the surface fluorescence maps and derived indices for vegetation status monitoring. Level 3 products will regard spatial mosaics (regional, continental and global scale) and temporal composites (monthly, seasonal and annual). The Level 4 will be the higher level products after the assimilation of fluorescence and canopy variables within dynamical vegetation models for the generation of gross primary productivity maps.

The spectral fitting based algorithms proposed in this work form part of the entire processing needed for converting Level 1 to Level 2 products. A synthetic flowchart of the retrieval scheme for FLEX, starting from the top of atmosphere radiance (Level 1) up to the surface reflectance and fluorescence spectrum (Level 2a) is summarized in Figure 13. As mentioned earlier, the atmospheric correction process relies also on the S3 data that provide valuable information to constrain the atmospheric parameter retrieval. The resulting bottom of atmosphere radiance is thus decomposed into its reflected and fluorescence components.

<Figure 13>

Finally, a number of indices can be routinely derived from the full fluorescence spectrum facilitating the exploitation of the spectral information. In addition to fluorescence values at the $O_2$ bands ($SIF_{687nm}$; $SIF_{760nm}$) which are useful for comparing SIF maps derived from FLEX with maps derived by others methods and sensors (usually centered at 687 and 760 nm), a number of other parameters informative of plant's activity and physiological status can be extracted at characteristic wavelengths (Table 6). For example, the SIF radiance at the maximum of the two emission peaks (*max*$SIF_{red}$; *max*$SIF_{far\text{-}red}$), the wavelength where the maximum of the emission peaks occurs (*max*$\lambda_{red}$, *max*$\lambda_{far\text{-}red}$), the radio between the red and far-red emission peaks (*ratio*SIF), and the spectrally integrated SIF emission (*int*SIF).

<Table 6>

## 6 Conclusions

The development and testing of fluorescence retrieval algorithms suitable for the FLEX mission, and for general application in future space missions, have been investigated in this study. Two major spectral fitting approaches have been considered: i) the retrieval at the $O_2$ absorption bands; and ii) the retrieval of the full fluorescence emission spectrum by a novel algorithm. The algorithms have been tested on a state-of-the-art dataset of RT simulations resampled according to the current technical specification of the FLORIS space-borne sensor. For the first time, the RT calculations include a more realistic coupling between the canopy and atmospheric directional effects. The latter resulted in one of the major sources of error in the retrieval. In particular, the retrieval at the $O_2$-A band was severely affected by the directional effects, while the analysis at $O_2$-B band showed less sensitivity. Therefore, further studies are needed to better understand and quantify the impact of directional effects on the total error budget and the opportunity of applying the SIF retrieval scheme at TOA level (where the directional effects are larger) will be evaluated. Nevertheless, the results presented suggest the possibility of retrieving red SIF with a high level of accuracy from the FLORIS sensor. The use of mathematical functions able to accurately model SIF and $\rho$ spectral behaviors, combined with the SR and SNR provided by the FLORIS sensor permitted of retrieving red SIF with a high level of accuracy.

The performance of the novel *SpecFit* retrieval algorithm is similar (and sometimes better) than those obtained with SFM at the $O_2$-A and $O_2$-B bands. The promising results achieved open new perspectives for further investigating the full fluorescence spectrum in relation to plant species and traits analysis, environmental conditions, structural and physiological variables, photosynthetic rates and stress occurrences. The proposed algorithm can be further optimized to retrieve SIF from high-resolution field spectroscopy measurements (Cogliati et al., 2015; Corp et al., 2010; Daumard et al., 2012; Meroni et al., 2008; Rossini et al., 2010) providing ground-based measurements useful to interpret satellite remote sensing observations.

However, the results presented here for both the retrieval approaches, cannot be representative of the true total error budget as expected from FLEX (i.e. from TOA radiance to canopy SIF) because an a-priori atmospheric correction was used. However, the FLEX End-to-End Simulator under development will enable a complete understanding of the retrieval error (from TOA radiance to surface reflectance and fluorescence), and the mission performance can be realistically investigated. Further instrument-related effects, such as smile, band broadening and stray-light, factors known to affect the retrieval accuracy and which are neglected in this study. This is because they will be minimized by sensor design, high-quality optics, and by controlling the cleanliness during the instrument manufacturing phase.

In summary, we have demonstrated the potential to retrieve the full spectrum of fluorescence from hyperspectral observations which can open new applications for better understanding of the terrestrial environment and ecosystem function.

## ACKNOWLEDGMENTS

This work was made possible by the funding support of the ESA project FLEX/S3 Tandem Mission Performance Analysis and Requirements Consolidation Study (PARCS) through ESA ESTEC contract no. 4000105078/11/NL/AF.

## REFERENCES


Agati, G. (1998). Response of the in vivo chlorophyll fluorescence spectrum to environmental factors and laser excitation wavelength. *Pure and Applied Optics: Journal of the European Optical Society Part A*, *7*(4), 797.

Baker, N. R. (2008). Chlorophyll Fluorescence: A Probe of Photosynthesis In Vivo. *Annual Review of Plant Biology*, *59*(1), 89–113. doi:10.1146/annurev.arplant.59.032607.092759

Berk, A., Anderson, G. P., Acharya, P. K., & Shettle, E. P. (2011). MODTRAN 5.2.1 User's Manual. Spectral Sciences, Inc., 4 Fourth Ave., Burlington, MA 01803-3304, Air Force Research Laboratory, Space Vehicles Directorate, Air Force Materiel Command, Hanscom AFB, MA 01731-3010.

Cogliati, S., Rossini, M., Julitta, T., Meroni, M., Schickling, A., Burkart, A., … Colombo, R. (2015). Continuous and long-term measurements of reflectance and sun-induced chlorophyll fluorescence by using novel automated field spectroscopy systems. *Remote Sensing of Environment*, *164*, 270–281. doi:10.1016/j.rse.2015.03.027

Corp, L. A., Cook, B. D., Middleton, E. M., Cheng, Y.-B., Huemmrich, K. F., & Campbell, P. K. E. (2010). Fusion: A f□ully u□ltraportable s□ystem for i□maging o□bjects in n□ature. In *2010 IEEE International Geoscience and Remote Sensing Symposium* (pp. 1671–1674). IEEE. doi:10.1109/IGARSS.2010.5652788

Daumard, F., Goulas, Y., Champagne, S., Fournier, A., Ounis, A., Olioso, A., & Moya, I. (2012). Continuous monitoring of canopy level sun-induced chlorophyll fluorescence during the growth of a sorghum field. *IEEE Transactions on Geoscience and Remote Sensing*, *50*(11 PART1), 4292–4300.

Donlon, C., Berruti, B., Buongiorno, A., Ferreira, M.-H., Féménias, P., Frerick, J., … Sciarra, R. (2012). The Global Monitoring for Environment and Security (GMES) Sentinel-3 mission. *Remote Sensing of Environment*, *120*, 37–57. doi:10.1016/j.rse.2011.07.024

ESA. (2015). Report for Mission Selection: FLEX. *ESA SP-1330/2 (2 volumes series)*, European Space Agency, Noordwijk, The Netherlands.

Franck, F., Juneau, P., & Popovic, R. (2002). Resolution of the Photosystem I and Photosystem II contributions to chlorophyll fluorescence of intact leaves at room temperature. *Biochimica et Biophysica Acta (BBA) - Bioenergetics*, *1556*(2-3), 239–246. doi:10.1016/S0005-2728(02)00366-3

Frankenberg, C., Fisher, J. B., Worden, J., Badgley, G., Saatchi, S. S., Lee, J.-E., … Yokota, T. (2011). New global observations of the terrestrial carbon cycle from GOSAT: Patterns of plant fluorescence with gross primary productivity. *Geophysical Research Letters*, *38*(17), n/a–n/a. doi:10.1029/2011GL048738

Frankenberg, C., Pollock, R., Lee, R. A. M., Rosenberg, R., Blavier, J.-F., Crisp, D., … Wunch, D. (2014). The Orbiting Carbon Observatory (OCO-2): spectrometer performance evaluation using pre-launch direct sun measurements. *Atmospheric Measurement Techniques Discussions*, *7*(7), 7641–7670. doi:10.5194/amtd-7-7641-2014

Gamon, J. A., Peñuelas, J., & Field, C. B. (1992). A narrow-waveband spectral index that tracks diurnal changes in photosynthetic efficiency. *Remote Sensing of Environment*, *41*(1), 35–44. doi:http://dx.doi.org/10.1016/0034-4257(92)90059-S

Guanter, L., Aben, I., Tol, P., Krijger, J. M., Hollstein, A., Köhler, P., … Landgraf, J. (2015). Potential of the TROPOspheric Monitoring Instrument (TROPOMI) onboard the Sentinel-5 Precursor for the monitoring of terrestrial chlorophyll fluorescence. *Atmospheric Measurement Techniques*, *8*(3), 1337–1352. doi:10.5194/amt-8-1337-2015

Guanter, L., Alonso, L., Gómez-Chova, L., Meroni, M., Preusker, R., Fischer, J., & Moreno, J. (2010). Developments for vegetation fluorescence retrieval from spaceborne high-resolution spectrometry in the O2-A and O2-B absorption bands. *Journal of Geophysical Research D: Atmospheres*, *115*(19).

Guanter, L., Frankenberg, C., Dudhia, A., Lewis, P. E., Gómez-Dans, J., Kuze, A., … Grainger, R. G. (2012). Retrieval and global assessment of terrestrial chlorophyll fluorescence from GOSAT space measurements. *Remote Sensing of Environment*, *121*, 236–251. doi:10.1016/j.rse.2012.02.006

Guanter, L., Zhang, Y., Jung, M., Joiner, J., Voigt, M., Berry, J. A., … Griffis, T. J. (2014). Global and time-resolved monitoring of crop photosynthesis with chlorophyll fluorescence. *Proceedings of the National Academy of Sciences of the United States of America*, *111* (14), E1327–33. doi:10.1073/pnas.1320008111

Hamazaki, T., Kaneko, Y., Kuze, A., & Kondo, K. (2005). Fourier transform spectrometer for Greenhouse Gases Observing Satellite (GOSAT). *Proc. SPIE*. doi:10.1117/12.581198

Joiner, J., Guanter, L., Lindstrot, R., Voigt, M., Vasilkov, A. P., Middleton, E. M., … Frankenberg, C. (2013). Global monitoring of terrestrial chlorophyll fluorescence from moderate-spectral-resolution near-infrared satellite measurements: methodology, simulations, and application to GOME-2. *Atmospheric Measurement Techniques*, *6*(10), 2803–2823. doi:10.5194/amt-6-2803-2013

Joiner, J., Yoshida, Y., Vasilkov, A. P., Corp, L. A., & Middleton, E. M. (2011). First observations of global and seasonal terrestrial chlorophyll fluorescence from space. *Biogeosciences*, *8*(3), 637–651. doi:10.5194/bg-8-637-2011

Joiner, J., Yoshida, Y., Vasilkov, A. P., Middleton, E. M., Campbell, P. K. E., Kuze, A., & Corp, L. A. (2012). Filling-in of near-infrared solar lines by terrestrial fluorescence and other geophysical effects: Simulations and space-based observations from SCIAMACHY and GOSAT. *Atmospheric Measurement Techniques*, *5*(4), 809–829. doi:10.5194/amt-5-809-2012

Kraft, S., Bezy, J.-L., Del Bello, U., Berlich, R., Drusch, M., Franco, R., … Silvestrin, P. (2013). FLORIS: Phase a status of the fluorescence imaging spectrometer of the earth explorer mission Candidate FLEX. In *Proceedings of SPIE - The International Society for Optical Engineering* (Vol. 8889).

Kraft, S., Del Bello, U., Bouvet, M., Drusch, M., & Moreno, J. (2012). FLEX: ESA's Earth Explorer 8 candidate mission. In *Geoscience and Remote Sensing Symposium (IGARSS), 2012 IEEE International* (pp. 7125–7128). doi:10.1109/IGARSS.2012.6352020

Kuze, A., Suto, H., Nakajima, M., & Hamazaki, T. (2009). Thermal and near infrared sensor for carbon observation Fourier-transform spectrometer on the Greenhouse Gases Observing Satellite for greenhouse gases monitoring. *Applied optics*, *48*(35), 6716–33. doi:10.1364/AO.48.006716

Lee, J.-E., Berry, J. A., van der Tol, C., Yang, X., Guanter, L., Damm, A., … Frankenberg, C. (2015). Simulations of chlorophyll fluorescence incorporated into the Community Land Model version 4. *Global Change Biology*, n/a–n/a. doi:10.1111/gcb.12948

Lee, J.-E., Frankenberg, C., Van Der Tol, C., Berry, J. A., Guanter, L., Boyce, C. K., … Saatchi, S. (2013). Forest productivity and water stress in Amazonia: Observations from GOSAT chlorophyll fluorescence. *Tohoku Journal of Experimental Medicine*, *230*(1).

Mazzoni, M., Falorni, P., & Del Bianco, S. (2008). Sun-induced leaf fluorescence retrieval in the O2-B atmospheric absorption band. *Optics Express*, *16*(10), 7014–7022.

Mazzoni, M., Falorni, P., & Verhoef, W. (2010). High-resolution methods for fluorescence retrieval from space. *Optics Express*, *18*(15), 15649–15663. doi:10.1364/OE.18.015649

Mazzoni, M., Meroni, M., Fortunato, C., Colombo, R., & Verhoef, W. (2012). Retrieval of maize canopy fluorescence and reflectance by spectral fitting in the O 2-A absorption band. *Remote Sensing of Environment*, *124*, 72–82. doi:10.1016/j.rse.2012.04.025

Meroni, M., Busetto, L., Colombo, R., Guanter, L., Moreno, J., & Verhoef, W. (2010). Performance of Spectral Fitting Methods for vegetation fluorescence quantification. *Remote Sensing of Environment*, *114*(2), 363–374. doi:http://dx.doi.org/10.1016/j.rse.2009.09.010

Meroni, M., Rossini, M., Picchi, V., Panigada, C., Cogliati, S., Nali, C., & Colombo, R. (2008). Assessing steady-state fluorescence and PRI from hyperspectral proximal sensing as early indicators of plant stress: The case of ozone exposure. *Sensors*, *8*(3), 1740–1754. doi:10.3390/s8031740

Nicodemus, F. E. (1977). Geometrical considerations and nomenclature for reflectance. Washington: U.S. Dept. of Commerce, National Bureau of Standards□: for sale by the Supt. of Docs., U.S. Govt. Print. Off.

Papageorgiou, G. C., & Govindjee. (2004). Chlorophyll a fluorescence: a signature of photosynthesis. *Advances in Photosynthesis and Respiration*, *19*.

Parazoo, N. C., Bowman, K., Fisher, J. B., Frankenberg, C., Jones, D. B. A., Cescatti, A., … Montagnani, L. (2014). Terrestrial Gross Primary Production Inferred From Satellite Fluorescence and Vegetation Models. *Global change biology*. doi:10.1111/gcb.12652

Rossini, M., Meroni, M., Migliavacca, M., Manca, G., Cogliati, S., Busetto, L., … Colombo, R. (2010). High resolution field spectroscopy measurements for estimating gross ecosystem production in a rice field. *Agricultural and Forest Meteorology*, *150*(9), 1283–1296. doi:10.1016/j.agrformet.2010.05.011

Stancik, A. L., & Brauns, E. B. (2008). A simple asymmetric lineshape for fitting infrared absorption spectra. *Vibrational Spectroscopy*, *47*(1), 66–69. doi:10.1016/j.vibspec.2008.02.009

Van Der Tol, C., Verhoef, W., Timmermans, J., Verhoef, A., & Su, Z. (2009). An integrated model of soil-canopy spectral radiances, photosynthesis, fluorescence, temperature and energy balance. *Biogeosciences*, *6*(12), 3109–3129. doi:10.5194/bg-6-3109-2009

Van Wittenberghe, S., Alonso, L., Verrelst, J., Hermans, I., Delegido, J., Veroustraete, F., … Samson, R. (2013). Upward and downward solar-induced chlorophyll fluorescence yield indices of four tree species as indicators of traffic pollution in Valencia. *Environmental pollution (Barking, Essex : 1987)*, *173*, 29–37. doi:10.1016/j.envpol.2012.10.003

Verhoef, W., & Bach, H. (2007). Coupled soil–leaf-canopy and atmosphere radiative transfer modeling to simulate hyperspectral multi-angular surface reflectance and {TOA} radiance data. *Remote Sensing of Environment*, *109*(2), 166–182. doi:http://dx.doi.org/10.1016/j.rse.2006.12.013

Verhoef, W., & Bach, H. (2012). Simulation of Sentinel-3 images by four-stream surface–atmosphere radiative transfer modeling in the optical and thermal domains. *Remote Sensing of Environment*, *120*, 197–207. doi:10.1016/j.rse.2011.10.034

Verhoef, W., van der Tol, C., & Middleton, E. M. (2014). Vegetation canopy fluorescence and reflectance retrieval by model inversion using optimization. In *5th International Workshop on Remote Sensing of Vegetation Fluorescence, 22-24 April 2014, Paris (France).*

Zhao, F., Guo, Y., Verhoef, W., Gu, X., Liu, L., & Yang, G. (2014). A Method to Reconstruct the Solar-Induced Canopy Fluorescence Spectrum from Hyperspectral Measurements. *Remote Sensing*, *6*(10), 10171–10192. doi:10.3390/rs61010171

**FIGURE CAPTIONS**

**Figure 1:** Typical spectra of top of atmosphere radiance as detected by the FLORIS-WBS (gray) and NBS (blue) (stacked for clarity), sun-induced fluorescence (red) and reflectance (green) are shown in the upper plot. Details of the high-resolution FLORIS-NBS spectra at the $O_2$-B (left) and $O_2$-A (right) are depicted in the bottom plots.

**Figure 2:** Atmospheric transfer functions used in the forward model for calculating top of atmosphere radiance (left table), the angular brakets represent the spectral convolution to the sensor spectral bands. Typical spectra of the atmospheric transfer functions used in the forward radiative transfer model are shown in the 500-780 nm spectral range (rigth plot).

**Figure 3:** Range of variations of reflectance (left), fluorescence (middle) and at sensor radiance radiance (rigth) of the 31 simulated cases.

**Figure 4:** Average RMSE over the 31 simulated cases at the $O_2$-A (left) and $O_2$-B (right) bands for the broader spectral window. The colors refer to three major classes of functions: i) polynomial (red); ii) Legendre polynomial (blue); and iii) piecewise cubic splines (green). The different SFM versions (1-18) are on the abscissa. The box center is the median, the edges the 25$^{th}$ and 75$^{th}$ percentiles and the whiskers extend to the most extreme data points. The scale limit settled at 1 mW m$^{-2}$ sr$^{-1}$ nm$^{-1}$ to highlight results with higher accuracies, while larger RMSE are grouped on top.

**Figure 5:** SIF retrieval accuracy in terms of RMSE (top), RRMSE% (middle) and $SIF_{diff}$ (bottom) at the $O_2$-A (blue) and $O_2$-B (red) bands by means of SFM version 18-S. Cases 1-19 and 20-31 consider variation of surface and atmospheric parameters respetively.

**Figure 6:** Results achieved by using SFM at the $O_2$-A band. The spectra for one of the better results (case 17), and for one of the worst results (case 30), are shown on the left and right, respectively. The upper plots show the reflectance quantities: $\rho$ is the target reflectance (blue), $\rho_{app}$ is the apparent reflectance (green), and $\rho_{ret}$ the retrieved one (red). The lower plots show the target (blue) and retrieved (red) SIF.

**Figure 7:** Four reflectance terms $r_{so}$ (blue), $r_{do}$ (green), $r_{sd}$ (red), $r_{dd}$ (gray) in the visible to near-infrared for the database cases 17 (left) and case 30 (rigth).

**Figure 8:** Spectral fitting retrieval at the $O_2$-B band for case 17. Left plot shows the target $\rho$ (blue), the apparent $\rho_{app}$ (green) and the retrieved $\rho_{ret}$ (red) reflectance. The right plot shows target (blue) and retrieved (red) SIF spectra.

**Figure 9:** Optimization of the piecewise cubic spline used for fitting surface reflectance. The left plot shows the RMSE for simulations 1-18 (where surface reflectance has been changed) considering different knots numbers (3-20 knots). The right plot shows a typical fitting of surface reflectance ($\rho$) by using piecewise cubic spline with 15 knots ($\rho_{spline}$).

**Figure 10:** Retrieval accuracies in terms of RMSE (top), RRMSE% (bottom) at the $O_2$-A (blue), $O_2$-B (red) and for the full fluorescence spectrum (green) achieved by SpecFit algorithm. The cases 1-19 consider variation of surface parameters, while cases 20-31 variations of atmospheric parameters.

**Figure 11:** Retrieval of full SIF spectrum with SpecFit algorithm in the 670-780 nm fitting range. The upper plots show target reflectance $\rho$ (blue), apparent reflectance $\rho_{app}$ (green), and retrieved reflectance $\rho_{ret}$ (red line). The charts on the bottom show target (blue) and retrieved (red) SIF spectra. The plots on the left and right refer to case 17 (i.e., better results) and case 30 (i.e., worse result) respectively.

**Figure 12:** Comparison between SIF values retrieved by spectral fitting at the $O_2$ bands (blue circles) and SpecFit (red squares). The target (SIF) and retrieved ($SIF_{ret}$) fluorescence values at 760 nm (left), 687 nm (center) and for the integral of the full SIF emission spectrum (right) obtained on the 31 RT simulations are shown. The gray dash-dot represents the 1:1 line.

**Figure 13:** Flow chart of the FLEX retrieval scheme from top of atmospfere radiance to the surface reflectance, fluorescence, and derived indices.

Table 1: Technical characteristics of the FLORIS spectra in terms of spectral resolution (SR), spectral sampling interval (SSI), and signal to noise ratio (SNR) for the different spectral regions.

| **Spectral Region** | **Visible** | **SIF$_{red}$** | | **red-edge** | | **SIF$_{far\text{-}red}$** | | | |
|---|---|---|---|---|---|---|---|---|---|
| **λ (nm)** | 500-677 | 677-686 | 686-697 | 697-740 | 740-755 | 755-759 | 759-762 | 762-769 | 769-780 |
| **SR (nm)** | 3.0 | 0.6 | 0.3 | 2.0 | 0.7 | | 0.3 | | 0.7 |
| **SSI (nm)** | 2.0 | 0.5 | 0.1 | 0.65 | 0.5 | | 0.1 | | 0.5 |
| **SNR** | 245 | 340 | 175 | 425 | linear from 510 to 1015 | 1015 | 115 | linear from 115 to 455 | 1015 |

Table 2: Surface and atmospheric parameters for SCOPE and MODTRAN radiative transfer models. The low, standard and high values used in the different cases simulated are reported. The right column “Coupling” indicates whether the parameters for the two models are coupled.

| **Case** | **Parameter** | **Unit** | **Values** | | | **Coupling** |
|---|---|---|---|---|---|---|
| | | | **low** | **medium** (case 19) | **high** | |
| **Surface parameters (SCOPE)** | | | | | | |
| 1-2 | Soil reflectance | | 1 | 2 | 3 | N |
| 3-4 | chlorophyll content (Cab) | $\mu g\ cm^{-2}$ | 20 | 40 | 80 | N |
| 5-6 | leaf water equivalent layer (Cw) | cm | 0.01 | 0.02 | 0.03 | N |
| 7-8 | dry matter content (Cdm) | $g\ cm^{-2}$ | 0.0025 | 0.005 | 0.01 | N |
| 9-10 | senescent material content (Cs) | - | 0.05 | 0.10 | 0.20 | N |
| 11-12 | maximum carboxylation capacity (Vcmax) | $\mu mol\ m^{-2}\ s^{-1}$ | 0 | 40 | 100 | N |
| 13-14 | stomatal conductance (m) | - | 2 | 5 | 9 | N |
| 15-16 | leaf area index (LAI) | | 0.5 | 2 | 8 | N |
| 17-18 | leaf inclination distribution function (LIDF) | | planophile | spherical | erectophile | N |
| **Atmospheric parameters (MODTRAN5)** | | | | | | |
| 20-21 | Surface height | m | 0 | 400 | 1200 | Y |
| 22-23 | Visibility | km | 5 | 20 | 80 | N |
| 24-25 | Humidity | | 0.5× | 1.0× | 2.0× | Y |
| 26-27 | Aerosol Type | | maritime | rural | urban | N |
| 28-29 | Profile | | mid-latitude winter | mid-latitude summer | tropical | Y |
| 30-31 | Solar zenith angle | deg | 30 | 45 | 60 | Y |

Table 3: Spectral windows at $O_2$-B and $O_2$-A bands tested with different spectral fitting algorithms.

| **spectral window** | **$O_2$-B** [nm] | **$O_2$-A** [nm] |
|---|---|---|
| **1** | 686-691 | 759-769 |
| **2** | 686-696 | 750-780 |

Table 4: Combinations of mathematical functions tested in the SFM algorithms to retrieve SIF and ρ.

| **Polynomial** | | | | **Legendre** | | | | **Spline** | | |
|---|---|---|---|---|---|---|---|---|---|---|
| **ID** | **ρ** | **SIF** | | **ID** | **ρ** | **SIF** | | **ID** | **ρ** | **SIF** |
| **1-P** | Linear | Linear | | **1-L** | Linear | Linear | | **1-S** | Linear | Linear |
| **2-P** | Quadratic | Linear | | **2-L** | Quadratic | Linear | | **2-S** | Quadratic | Linear |
| **3-P** | Cubic | Linear | | **3-L** | Cubic | Linear | | **3-S** | Cubic | Linear |
| **4-P** | Linear | Quadratic | | **4-L** | Linear | Quadratic | | **4-S** | Linear | Quadratic |
| **5-P** | Quadratic | Quadratic | | **5-L** | Quadratic | Quadratic | | **5-S** | Quadratic | Quadratic |
| **6-P** | Cubic | Quadratic | | **6-L** | Cubic | Quadratic | | **6-S** | Cubic | Quadratic |
| **7-P** | Linear | Cubic | | **7-L** | Linear | Cubic | | **7-S** | Linear | Cubic |
| **8-P** | Quadratic | Cubic | | **8-L** | Quadratic | Cubic | | **8-S** | Quadratic | Cubic |
| **9-P** | Cubic | Cubic | | **9-L** | Cubic | Cubic | | **9-S** | Cubic | Cubic |
| **10-P** | Linear | Gaussian | | **10-L** | Linear | Gaussian | | **10-S** | Linear | Gaussian |
| **11-P** | Quadratic | Gaussian | | **11-L** | Quadratic | Gaussian | | **11-S** | Quadratic | Gaussian |
| **12-P** | Cubic | Gaussian | | **12-L** | Cubic | Gaussian | | **12-S** | Cubic | Gaussian |
| **13-P** | Linear | Lorentzian | | **13-L** | Linear | Lorentzian | | **13-S** | Linear | Lorentzian |
| **14-P** | Quadratic | Lorentzian | | **14-L** | Quadratic | Lorentzian | | **14-S** | Quadratic | Lorentzian |
| **15-P** | Cubic | Lorentzian | | **15-L** | Cubic | Lorentzian | | **15-S** | Cubic | Lorentzian |
| **16-P** | Linear | Voigt | | **16-L** | Linear | Voigt | | **16-S** | Linear | Voigt |
| **17-P** | Quadratic | Voigt | | **17-L** | Quadratic | Voigt | | **17-S** | Quadratic | Voigt |
| **18-P** | Cubic | Voigt | | **18-L** | Cubic | Voigt | | **18-S** | Cubic | Voigt |

Table 5: Comparison between SFM and *SpecFit* algorithms at 760 nm, 687 nm and for the integral of the full fluorescence emission spectrum (670-780 nm) for the 31 cases. The retrieval accuracy in terms of: slope ($c_1$) and intercept ($c_2$) of the linear model, $r^2$ adjusted, RMSE ([mW $m^{-2}sr^{-1}nm^{-1}$] and [mW $m^{-2}sr^{-1}$] for values at the $O_2$ bands and spectral integral respectively), and RRMSE% are reported.

| | $SFM_{760nm}$ | $SFM_{687nm}$ | $SpecFit_{760nm}$ | $SpecFit_{687nm}$ | $SpecFit_{Int}$ |
|---|---|---|---|---|---|
| $c_1$ | 0.935* | 0.978* | 0.956* | 0.956* | 0.936* |
| $c_2$ | -0.007 | 0.035 | -0.012 | 0.081* | 1.663 |
| $r^2_{adj}$ | 0.98 | 0.99 | 0.97 | 0.99 | 0.97 |
| ***RMSE*** | 0.037 | 0.018 | 0.044 | 0.018 | 6.225 |
| ***RRMSE%*** | 7.4 | 3.0 | 6.2 | 2.9 | 6.4 |

* p-values < 0.05

Table 6: List of indices derived from the full fluorescence spectrum.

| **Derived products** | **Unit** | **Specification** |
|---|---|---|
| $SIF_{760nm}$ | mW $m^{-2}sr^{-1}nm^{-1}$ | Fluorescence at 760 nm |
| $SIF_{687nm}$ | mW $m^{-2}sr^{-1}nm^{-1}$ | Fluorescence at 687 nm |
| *max*$SIF_{far\text{-}red}$ | mW $m^{-2}sr^{-1}nm^{-1}$ | Fluorescence at the maximum of the far-red peak |
| *max*$SIF_{red}$ | mW $m^{-2}sr^{-1}nm^{-1}$ | Fluorescence at the maximum of the red peak |
| *max*$\lambda_{far\text{-}red}$ | nm | Wavelength of the maximum for far-red peak |
| *max*$\lambda_{red}$ | nm | Wavelength of the maximum for red peak |
| *ratio*SIF | - | *max*$SIF_{red}$ / *max*$SIF_{far\text{-}red}$ |
| *Int*SIF | mW $m^{-2}sr^{-1}$ | Integral of the full SIF emission |

**Figure 1 (size 2-column)**

**Click here to download high resolution image**

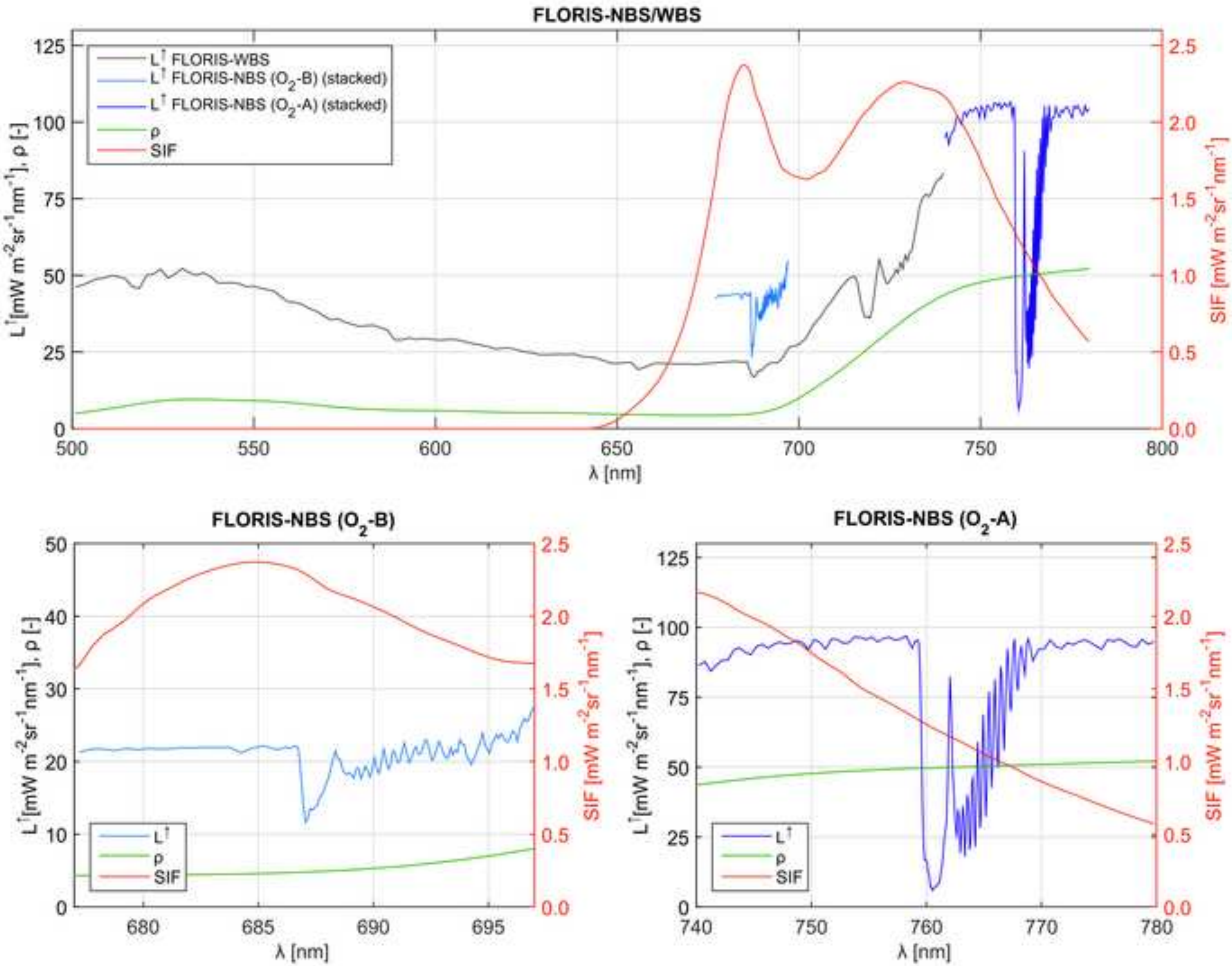

**Figure 2 (size 1.5-column)**
**Click here to download high resolution image**

| *Atmospheric Functions* | *Name* |
|---|---|
| $\langle E_s^0 \rangle \cos\theta_s / \pi$ | $t_1$ |
| $\langle \rho_{so} \rangle$ | $t_2$ |
| $\langle \rho_{dd} \rangle$ | $t_3$ |
| $\langle \tau_{ss} \rangle$ | $t_4$ |
| $\langle \tau_{sd} \rangle$ | $t_5$ |
| $\langle \tau_{oo} \rangle$ | $t_6$ |
| $\langle \tau_{do} \rangle$ | $t_7$ |
| $\langle \tau_{ss} \tau_{oo} \rangle$ | $t_8$ |
| $\langle \tau_{sd} \tau_{oo} \rangle$ | $t_9$ |
| $\langle \tau_{ss} \tau_{do} \rangle$ | $t_{10}$ |
| $\langle \tau_{sd} \tau_{do} \rangle$ | $t_{11}$ |
| $\langle \tau_{ss} \rho_{dd} \rangle$ | $t_{12}$ |
| $\langle \rho_{dd} \tau_{oo} \rangle$ | $t_{13}$ |
| $\langle \tau_{ss} \rho_{dd} \tau_{oo} \rangle$ | $t_{14}$ |

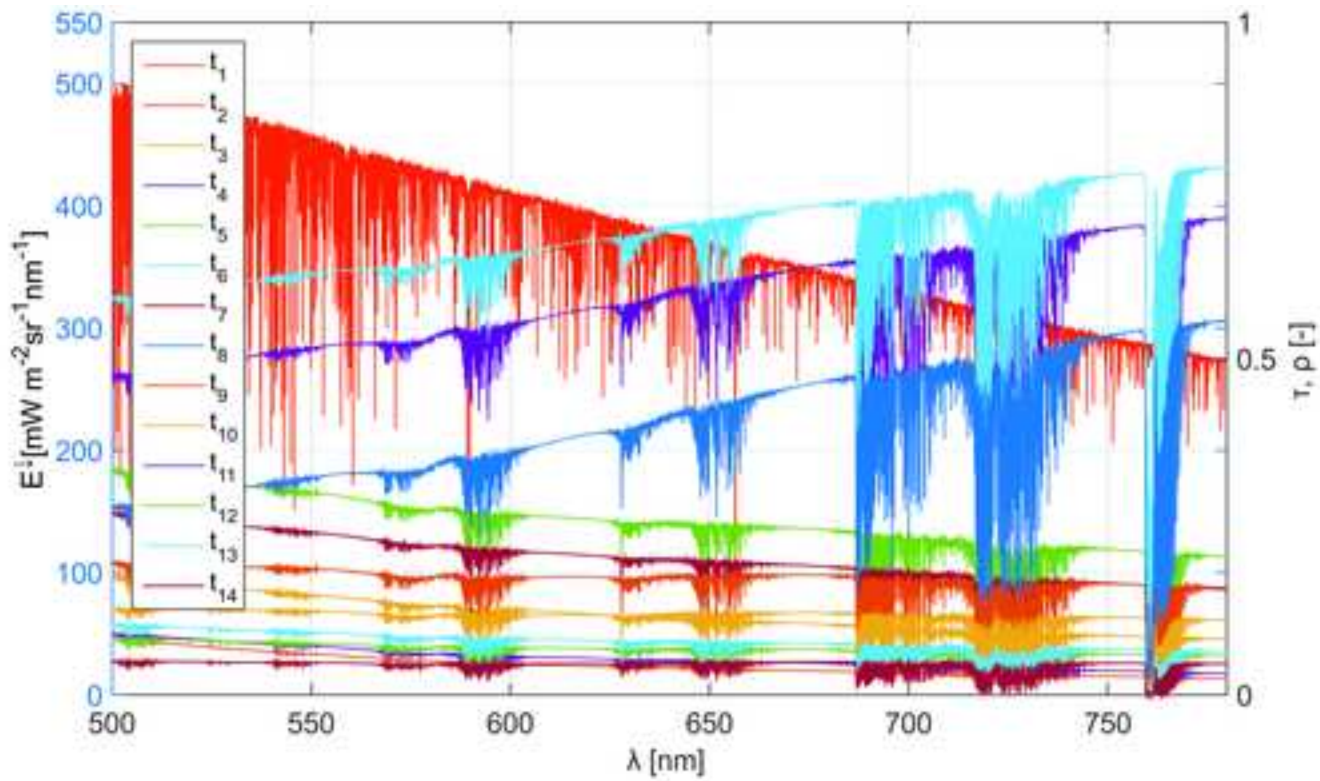

Figure 3 (size 1.5-column)
Click here to download high resolution image

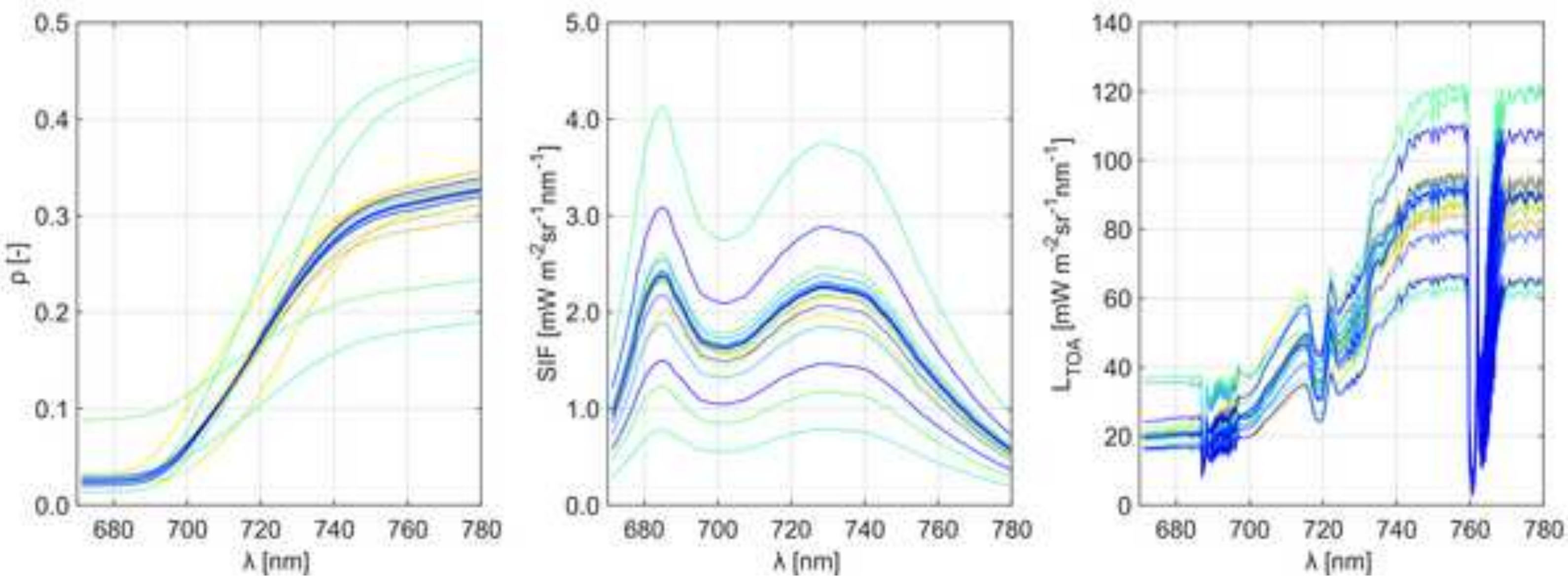

Figure 4 (size single -column)
Click here to download high resolution image

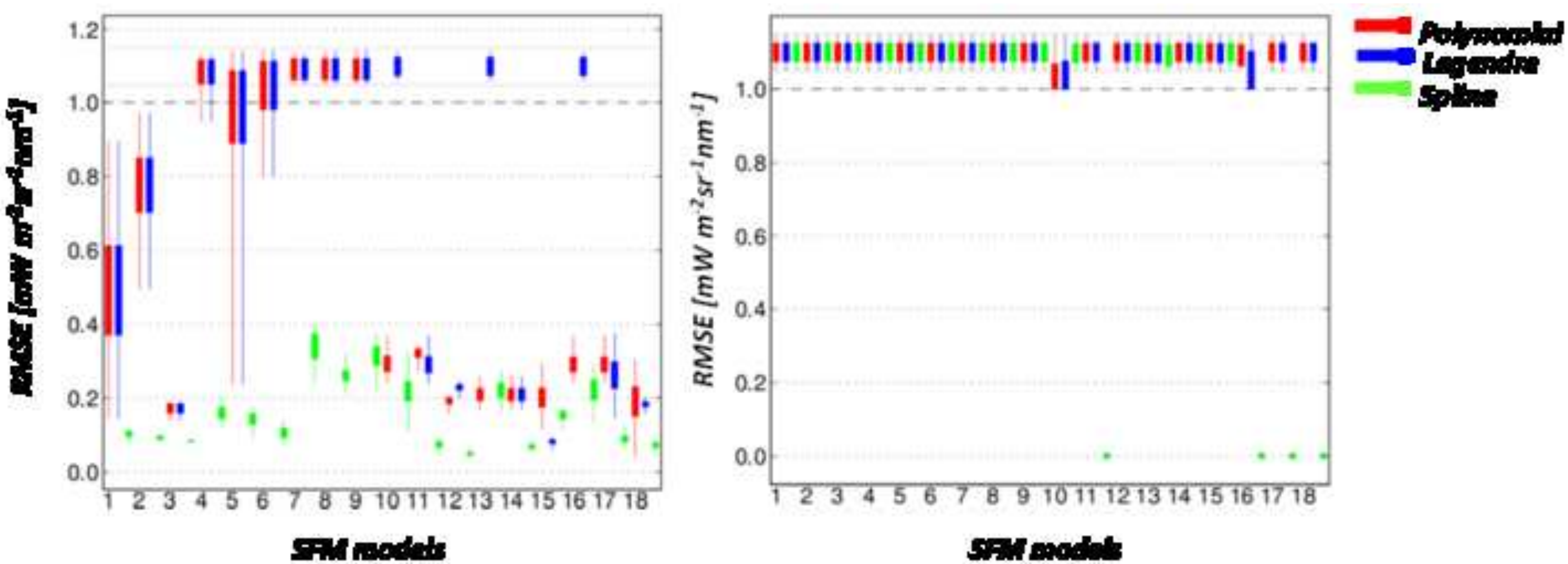

**Figure 5 (size single -column)**

**Click here to download high resolution image**

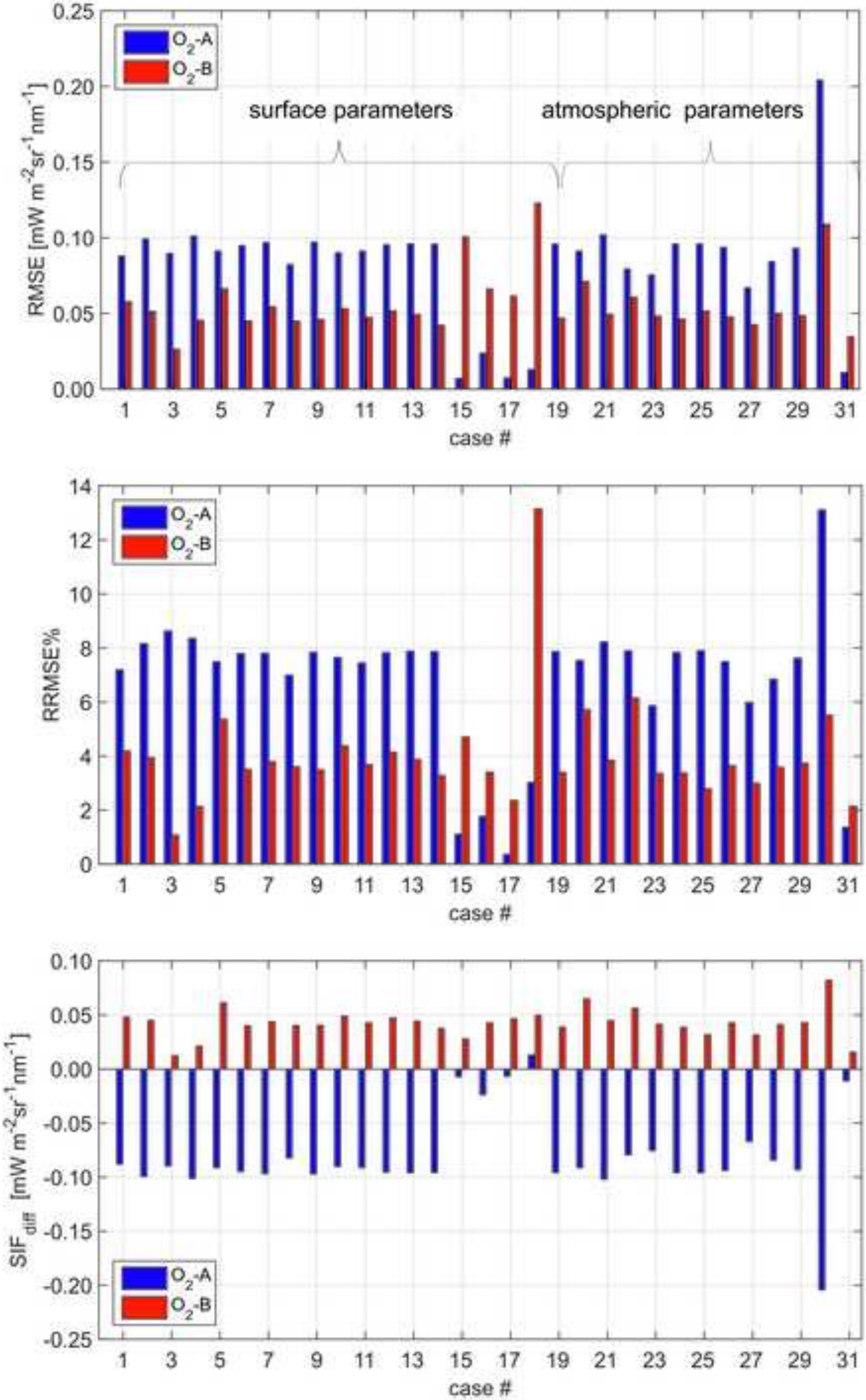

**Figure 6 (size 1.5 -column)**

**Click here to download high resolution image**

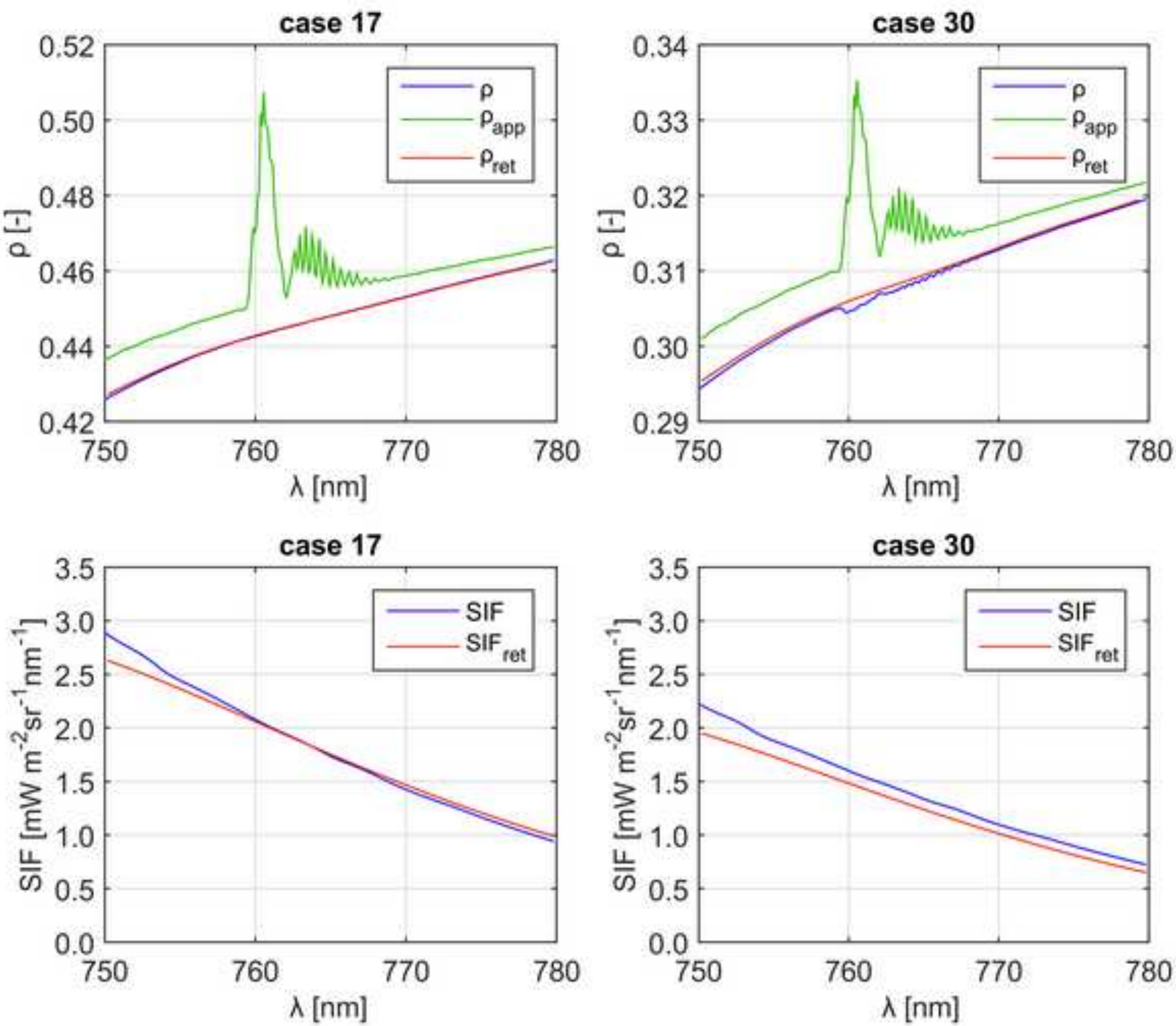

Figure 7 (size single -column)
Click here to download high resolution image

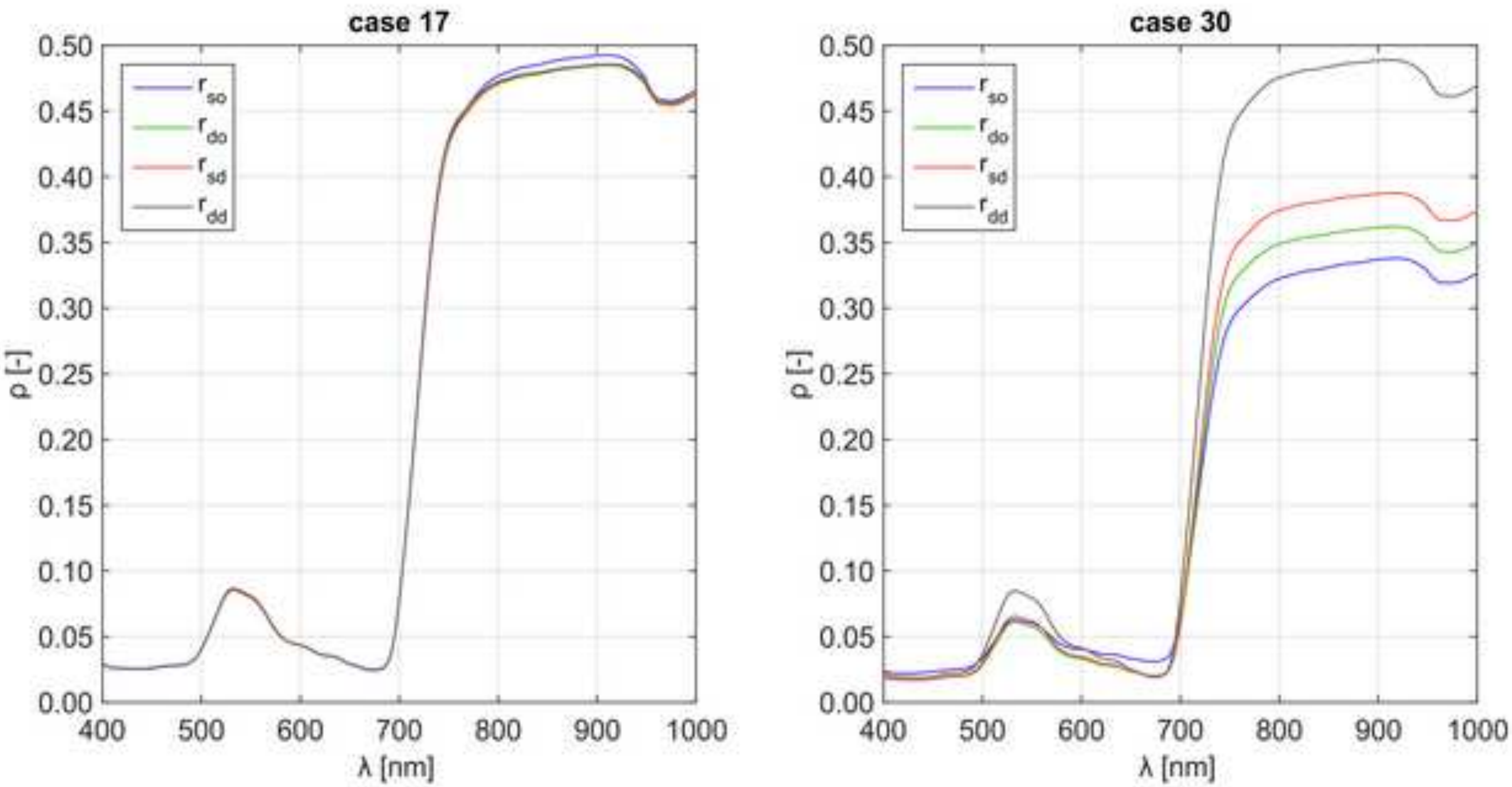

Figure 8 (size 1.5-column)
Click here to download high resolution image

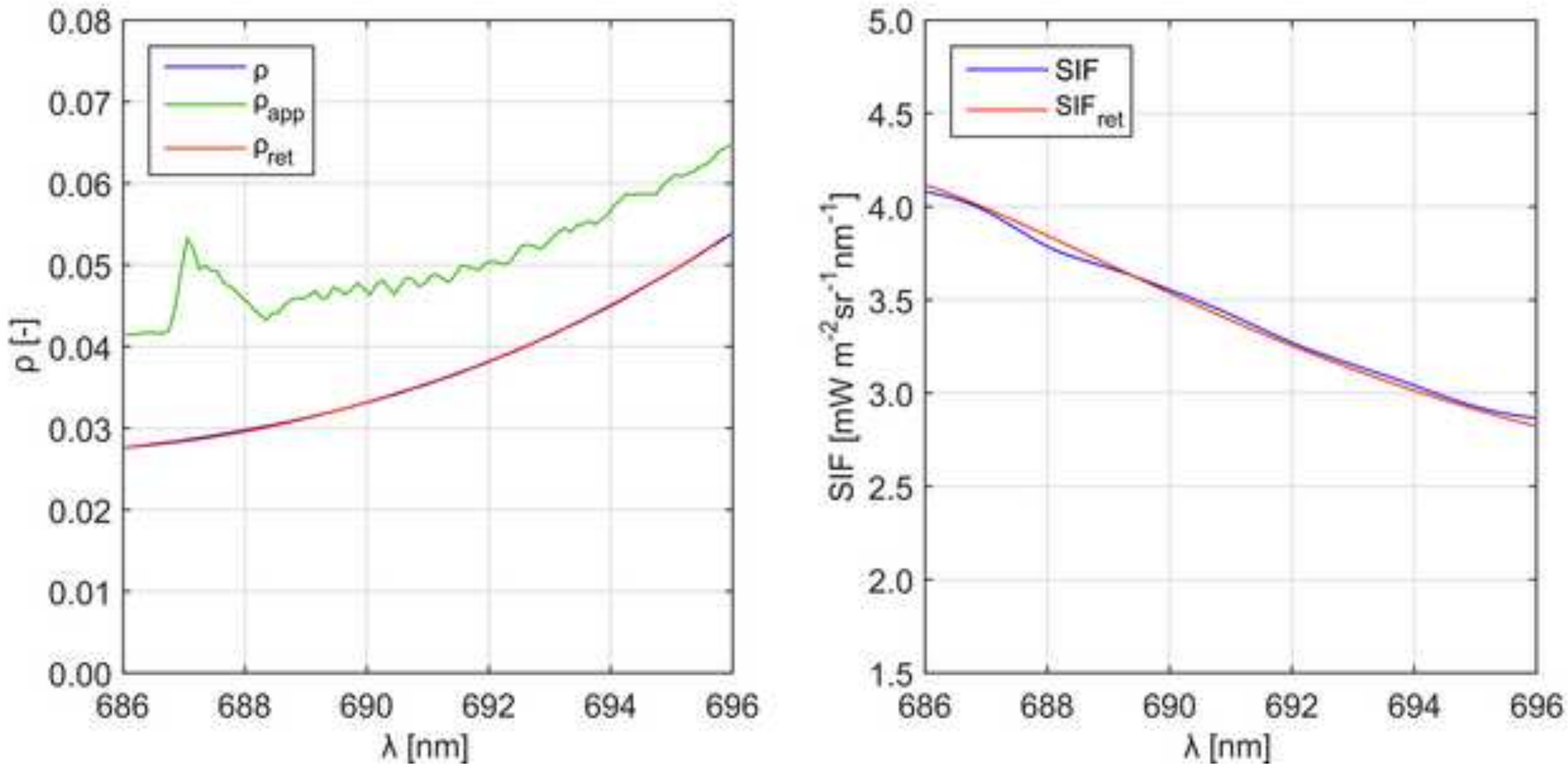

Figure 9 (size single-column)
Click here to download high resolution image

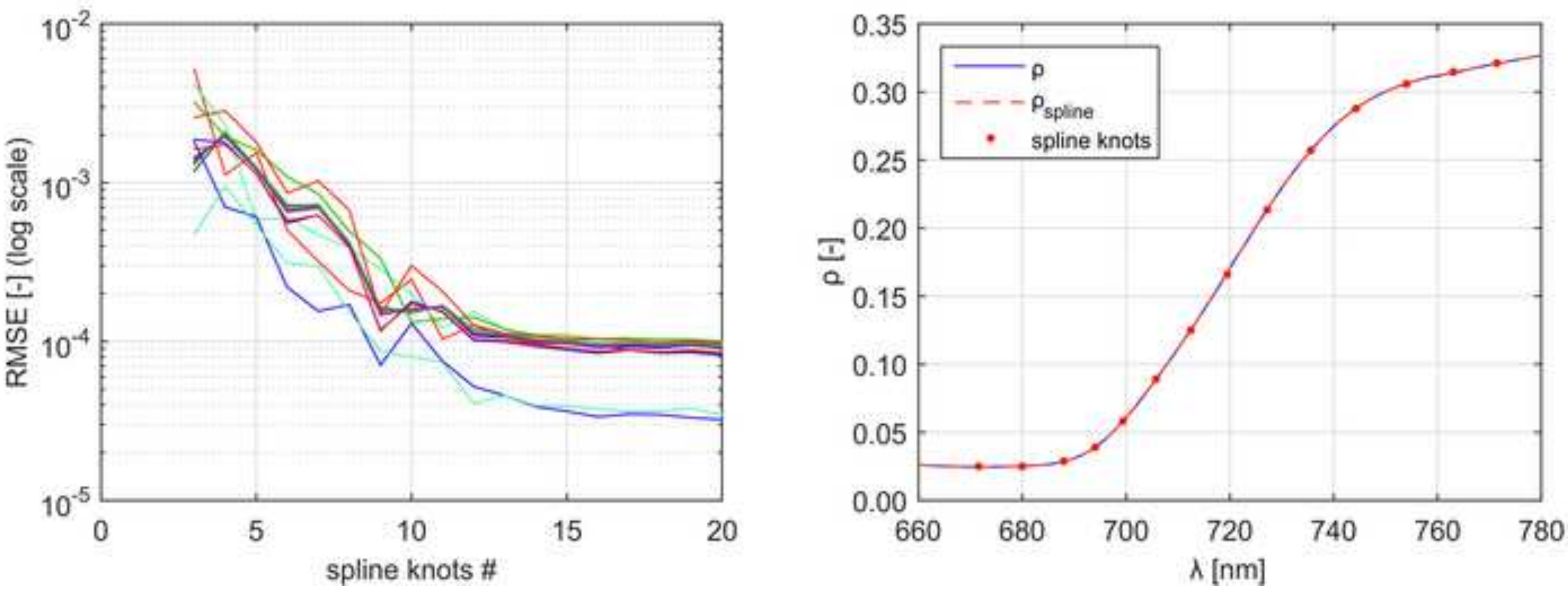

**Figure 10 (size single-column)**
Click here to download high resolution image

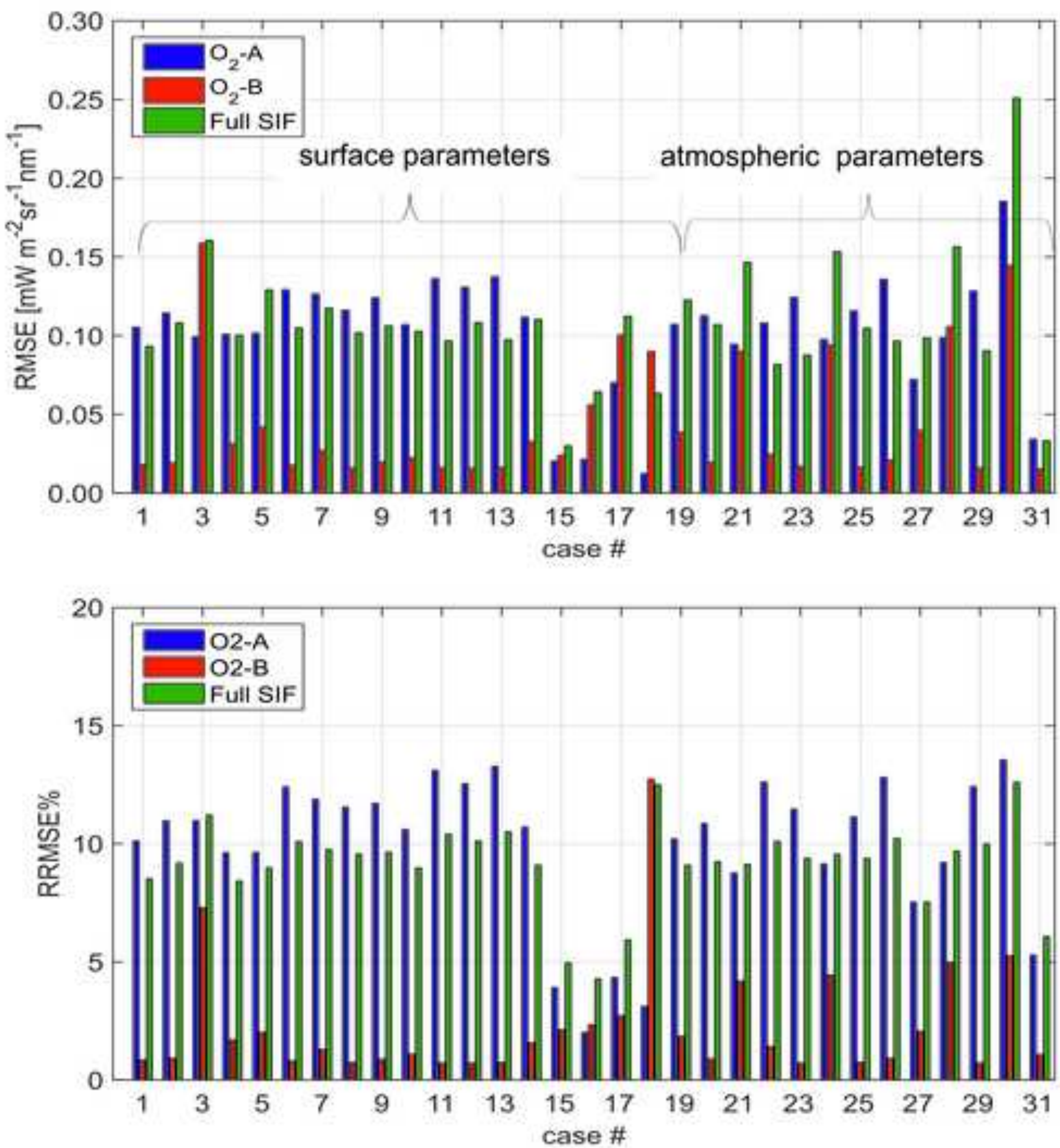

**Figure 11 (size 1.5-column)**

Click here to download high resolution image

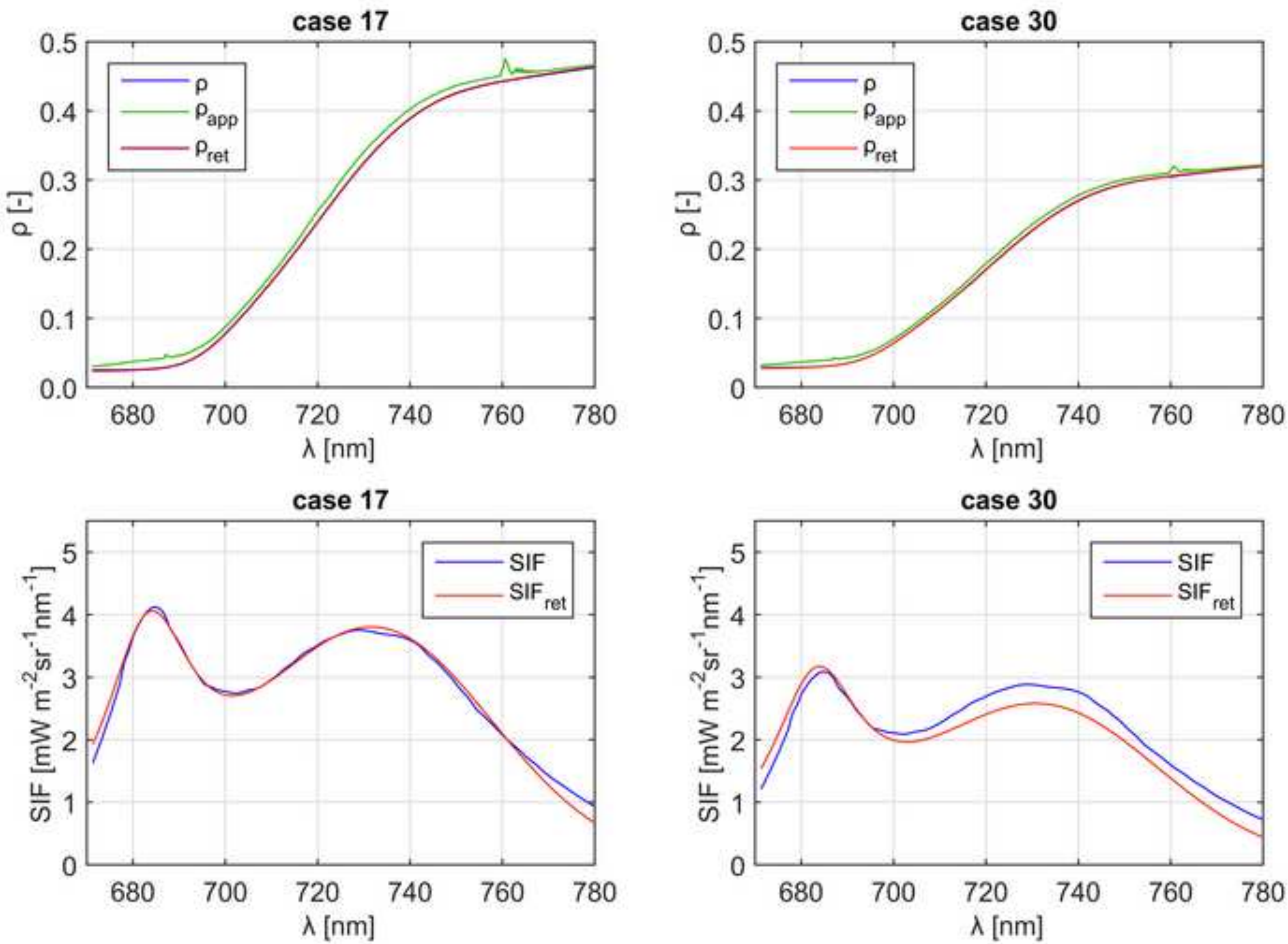

Figure 12 (size 1.5-column)

Click here to download high resolution image

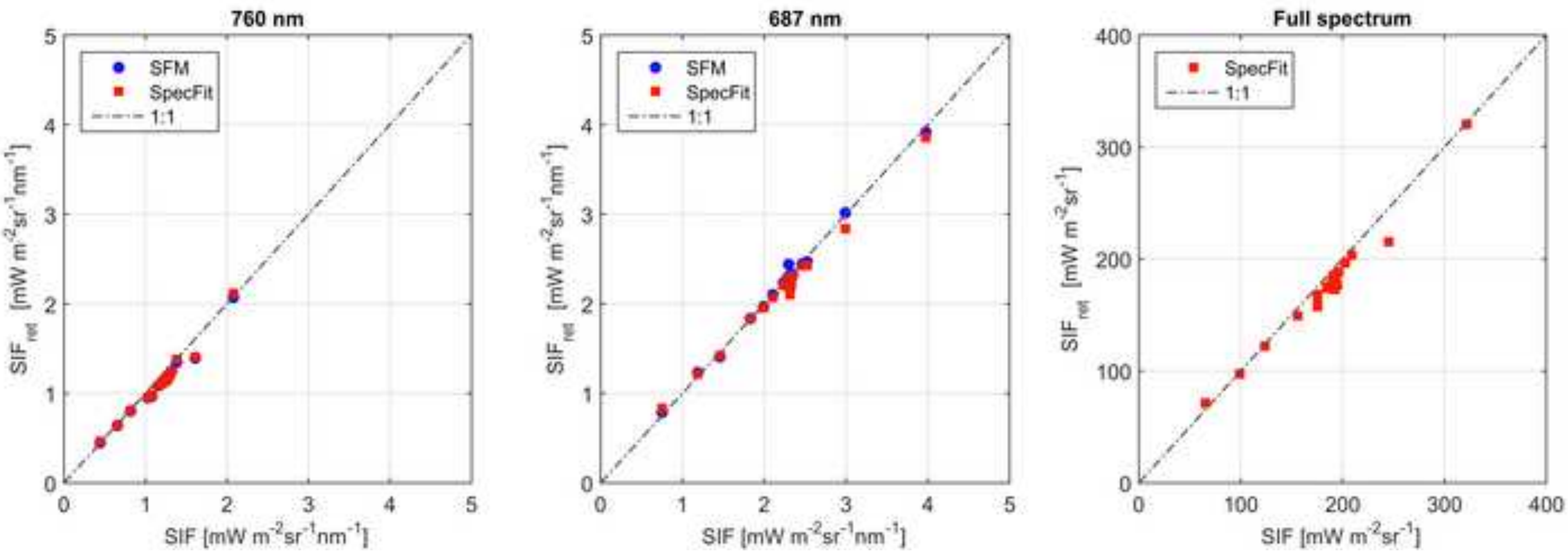

Figure 13 (size single-column)

Click here to download high resolution image